Research Square

Preprints are preliminary reports that have not undergone peer review.
They should not be considered conclusive, used to inform clinical practice,
or referenced by the media as validated information.

Lineage identity governs oncogene dependence in murine NSCLC models of KRAS inhibitor resistance

Tyler Jacks

t.jacks@mit.edu

David H. Koch Institute for Integrative Cancer Research https://orcid.org/0000-0001-5785-8911

Nicolas Mathey-Andrews

David H. Koch Institute for Integrative Cancer Research

Carrie Rodriguez

David H. Koch Institute for Integrative Cancer Research

Bing Shui

David H. Koch Institute for Integrative Cancer Research https://orcid.org/0000-0002-5956-130X

Agata Patriotis

David H. Koch Institute for Integrative Cancer Research https://orcid.org/0000-0002-8237-975X

William Rideout

David H. Koch Institute for Integrative Cancer Research

Victor Chen

Emory University

Ileana Murazzi

Herbert Irving Comprehensive Cancer Center, Columbia University

Milton Cornwall-Brady

David H. Koch Institute for Integrative Cancer Research https://orcid.org/0000-0002-7775-0606

Manyuan Liu

Herbert Irving Comprehensive Cancer Center, Columbia University

Morgan Heileman

David H. Koch Institute for Integrative Cancer Research

Marianna Trakala

David H. Koch Institute for Integrative Cancer Research

Carla Concepcion

Herbert Irving Comprehensive Cancer Center, Columbia University

Dian Yang

Herbert Irving Comprehensive Cancer Center, Columbia University

Article

Keywords:

Posted Date: July 24th, 2025

DOI: https://doi.org/10.21203/rs.3.rs-7058952/v1

License: This work is licensed under a Creative Commons Attribution 4.0 International License.
Read Full License

Additional Declarations: Yes there is potential Competing Interest. N.M.A. has served as an Ad Hoc consultant for Longitude Capital on matters unrelated to the content of this manuscript. D.Y. is a co-founder and consultant for DEM Biopharma. T.J. is a member of the Board of Directors of Amgen and Thermo Fisher Scientific, a co-Founder of Dragonfly Therapeutics and T2 Biosystems. Amgen currently owns and markets sotorasib, the primary therapeutic compound used in this manuscript. Sotorasib was purchased from a third-party source, Selleck Chemicals, and the work was not performed as a sponsored research agreement. T.J. serves on the Scientific Advisory Board of Dragonfly Therapeutics, SQZ Biotech, and Skyhawk Therapeutics. T.J. is also the President of Break Through Cancer. His laboratory currently receives funding from the Lustgarten Foundation and Johnson & Johnson Lung Cancer Initiative, but this funding did not support the research described in this manuscript. The remaining authors declare no competing interests.

Version of Record: A version of this preprint was published at Nature Genetics on September 30th, 2026. See the published version at https://doi.org/10.1038/s41588-026-02768-8.

Lineage identity governs oncogene dependence in murine NSCLC models of KRAS inhibitor resistance

AUTHOR LIST

Nicolas Mathey-Andrews[1,2,3], Carrie L. Rodriguez[1,2], Bing Shui[1], Agata L. Patriotis[1], William M. Rideout III[1], Victor Z. Chen[4,5,6], Ileana Murazzi[4,6], Milton R. Cornwall-Brady[1], Manyuan Liu[5,6], Morgan G. Heileman[1], Marianna Trakala[1], Carla P. Concepcion[5,6], Dian Yang[4,5,6], Tyler Jacks[1,7]

Affiliations:

[1] David H. Koch Institute for Integrative Cancer Research, Massachusetts Institute of Technology, Cambridge, MA

[2] Department of Biology, Massachusetts Institute of Technology, Cambridge, MA

[3] Harvard Medical School, Boston, MA

[4] Department of Systems Biology, Vagelos College of Physicians & Surgeons, New York City, NY

[5] Department of Molecular Pharmacology & Therapeutics, Vagelos College of Physicians & Surgeons, Columbia University Irving Medical Center, New York NY

[6] Herbert Irving Comprehensive Cancer Center, Columbia University, New York City, NY

[7] Corresponding author

Abstract:

Primary and acquired resistance to targeted therapy represent significant challenges to durable treatment responses in cancer. In lung cancer and other cancer types, allele-specific and pan-KRAS inhibitors offer new promise, but these are hampered by incomplete responses as well as genetic and non-genetic mechanisms of acquired resistance. To model these mechanisms, we treat genetically engineered mouse models of *Kras*^{G12C}-driven lung cancer with sotorasib, a KRAS^{G12C} inhibitor, until the emergence of drug resistance. The initial response to sotorasib was rapid, but incomplete. Residual tumor burden transcriptionally resembled the alveolar type II cell, phenocopying residual disease signatures identified in patients treated with EGFR inhibitors. After continued sotorasib treatment, we observed diverse mechanisms of drug resistance *in vivo*, including genetic MAPK reactivation and lineage transformation from adenocarcinoma to squamous histology. Focusing mechanistic studies on squamous transformation, we showed that expression of the basal transcription factor *ΔNp63* is sufficient to rewire transformed alveolar organoids to a squamous state *in vitro*, conferring insensitivity to KRAS inhibition. *In vivo*, either ectopic expression of *Sox2* or loss of *Nkx2-1*, which are tolerated during *Kras*-driven tumorigenesis, poised tumors for squamous lineage commitment upon KRAS inhibition. Squamous-transformed tumors did not exhibit evidence of KRAS/MAPK reactivation, underscoring the role for lineage transcription factors and histologic transformation in mediating oncogene independence.

Main text:

Targeted therapies are a pillar of treatment for lung adenocarcinoma (LUAD). Small molecule tyrosine kinase inhibitors (TKIs) are FDA approved for use in EGFR, ALK, ROS1, MET, and BRAF-mutant tumors[1]. Recent structural insights into the allosteric switch II binding pocket of the KRAS oncoprotein led to the development of allele-specific covalent $KRAS^{G12C}$ inhibitors[2,3]. Two such drugs, sotorasib and adagrasib, are FDA-approved for the refractory setting after demonstrating 37.1% and 42.9% objective response rates (ORR)[4,5], respectively, in phase 2-3 trials. These represent a pharmacologic breakthrough in the treatment of KRAS-mutant lung cancer, which constitutes over 30% of LUAD[6].

While targeted therapies prolong survival in lung cancer patients, they are seldom curative. Molecular mechanisms of resistance are diverse[7]. Secondary somatic mutations may enable drug resistance by reactivating the targeted pathway. Illustrative examples in EGFR-mutant tumors include secondary oncogene mutations that abrogate drug binding[8] (e.g., $EGFR^{C797S}$), activating mutations in downstream effectors (e.g., $BRAF^{V600E}$), or parallel pathway activation[9] (e.g., MET amplification), all of which restore MAP kinase (MAPK) signaling. Detection of these mutations can guide clinical management. For instance, a patient with a secondary MET amplification might rationally receive a MET inhibitor[10,11]. In contrast, histologic transformation (HT) is a poorly understood mechanism of therapy resistance without obvious secondary clinical targets. Transformation from adenocarcinoma to small cell lung cancer (SCLC)[12,13], squamous cell carcinoma (LUSC)[14,15], and the epithelial to mesenchymal transition[16] mediate resistance to targeted therapy, but a molecular understanding of these transitions and how they confer oncogene independence remains elusive.

Data are emerging on clinical mechanisms of resistance to KRAS inhibitors. Both categories of resistance mechanisms: secondary mutations, such as KRAS codon 12 and switch II mutations, as well as histologic transformations have been described[15,17]. HT from adenocarcinoma to squamous cell carcinoma has been observed in patients who relapsed on adagrasib, and adenosquamous histology at diagnosis predicts poor response to KRAS inhibition[18,19]. Targeted sequencing in these patients has revealed no obvious acquired driver mutations, suggesting epigenetic cellular reprogramming. STK11 mutations may predispose KRAS-driven lung cancer to adenosquamous histology[18,20], but these transitions also occur in the absence of STK11 mutations, notably in TKI-resistant EGFR and ALK mutant lung cancer[14,21]. Altogether, mechanisms that drive this process and rational clinical targets for squamous-transformed tumors remain unknown.

To address these questions, we utilized autochthonous murine models of *$Kras^{G12C}$*-driven lung adenocarcinoma to characterize response and resistance to oncogenic KRAS inhibition. Sotorasib induced rapid but incomplete lung tumor regression, with remaining drug-tolerant persister cells transcriptionally resembling alveolar type II cells. Through prolonged *in vivo* treatment, we reproducibly generated drug-resistant tumors

through diverse mechanisms, including MAPK reactivation as well as MAPK-independent histologic transformation. Using *in vivo* functional genetic approaches including CRISPR knock-out and CRISPR activation (CRISPRa), we deconstructed elements of the adenocarcinoma to squamous cell carcinoma transition, identifying lineage transcription factors that define lineage commitment, plasticity, and response to therapy.

Results:

Sotorasib causes rapid but incomplete tumor regression

To model KRAS^{G12C}-mutant lung cancer, we crossed a Cre conditional *LSL-Kras^{G12C}* allele to floxed p53 alleles to generate *Kras^{G12C};Trp53$^{fl/fl}$* (K$_C$P) mice. Upon intratracheal infection with an adenoviral vector that restricts expression of Cre recombinase in alveolar type II cells (Ad5-SPC-Cre)[23], a known cell of origin in this model, K$_C$P mice developed autochthonous lung lesions that progressed to advanced adenocarcinoma over the course of several months (**Fig. 1a**). Consistent with the weaker oncogenicity of the *Kras^{G12C}* oncogene, K$_C$P animals exhibited lower tumor burden and reduced tumor number than *LSL-Kras^{G12D};Trp53$^{fl/fl}$* (KP) mice, which has been conventionally used as a LUAD model (**Supplemental Fig. 1a**)[24].

To characterize the effect of sotorasib on K$_C$P tumors, we performed micro-computed tomography (μCT) on mice 16- and 24-weeks post infection (p.i.), randomizing mice to either daily 30 mg/kg sotorasib or vehicle control (**Fig. 1a**). After two weeks of sotorasib treatment, longitudinal μCT and histologic analysis revealed significant tumor regression (**Supplementary Fig. 1b-c**). The majority of tumor regression occurred within the first week (**Supplementary Fig. 1d)**, with significant differences in tumor burden evident after only 72 hours (**Supplementary Fig. 1e**). Two weeks of sotorasib treatment produced residual tumors that exhibited suppressed MAPK signaling as assessed by phosphorylated ERK (pERK) immunohistochemistry, confirming on-target pathway inhibition (**Fig. 1b**). Residual sotorasib-treated tumors had a significantly lower proliferative index than vehicle-treated tumors (**Supplementary Fig. 1f**), but did not exhibit increased apoptosis or inflammatory infiltrate (**Supplementary Fig. 1g-h**), suggesting the presence of drug-tolerant persistent (DTP) cancer cells.

Residual cancer cells adopt an alveolar type II cell signature

To transcriptionally profile DTP disease, we performed single-cell mRNA sequencing (scRNA-seq) on FACS-sorted cancer cells from K$_C$P*;LSL-Cas9-P2A-eGFP* (K$_C$P Cas9) mice treated with sotorasib or vehicle for two weeks, using eGFP as a fluorescent reporter (**Supplementary Fig. 2a**). Prior scRNA-seq studies utilizing doxycycline-inducible shRNAs against *Kras* demonstrated alveolar type I (AT1) differentiation in response to KRAS inhibition[25]. To identify this cell state without over-clustering the data, we adjusted the coarseness of Leiden community detection to define 13 transcriptional clusters including one (cluster 8) defined by canonical AT1 marker genes (*Hopx, Ager,*

Clic5)[26] (**Supplementary Fig. 2b**, **Supplementary Table 4**). Additional transcriptional clusters recapitulated the cell states described in the KP model, annotated by applying gene signatures identified in prior scRNA-seq and lineage-tracing studies (**Fig. 1c, Supplementary Fig. 2c, Supplementary Table 4**)[27,28].

As expected, sotorasib-treated tumor cells showed decreased enrichment for a KRAS signaling gene signature (**Supplementary Fig 3a**). Vehicle-treated tumor cells occupied all annotated clusters with relatively even distribution, including clusters defined by markers of higher-grade tumors (*Lgals3, Vim, Clu)* (**Fig 1d**). Sotorasib-treated tumors, however, primarily occupied clusters 0, 5 and 10, which are defined by alveolar type II (AT2) cell markers (**Fig. 1d, Supplementary Fig. 3b**). Pseudo-bulk differential expression analysis revealed that the top differentially expressed genes in treated cells were markers associated with AT2 identity (*Sftpa1, Lyz2, Napsa)* (**Fig. 1e, Supplementary Fig. 3c,d, Supplementary Table 4**). Preranked gene set enrichment analysis using a cell-type signature database confirmed strong enrichment for AT2 cell identity compared to AT1 or club cells (**Fig. 1f, Supplementary Table 5)**. This was particularly notable in light of scRNA sequencing performed in human EGFR-mutant lung adenocarcinomas treated with EGFRi. In this study, an AT2 cell signature uniquely distinguished residual disease (RD) from treatment naïve (TN) tumors or progressive disease (PD)[29]. We scored our dataset for this human RD signature, and found enrichment in sotorasib-treated cells **(Fig. 1g, Supplementary Table 5**). Top differentially expressed genes in vehicle-treated cells were primarily ribosomal subunit genes (*Rps18, Rps24*) (**Supplementary Fig. 3c**). This ribosomal signature may reflect the anabolic demand of more proliferative tumor cells, and corroborates 'Ribosome-high' cell clusters enriched in *Kras*-intact cancer cells from earlier characterization of the KP model[25].

To corroborate the observed enrichment of a well-differentiated alveolar phenotype in treated tumors, we used an established convolutional neural network (CNN) algorithm[30] to grade tumors that persisted through treatment. Treated residual tumor lesions were primarily composed of lower grade adenomas (G1/G2) compared to advanced adenocarcinoma (G3/G4) (**Fig. 1h**). In the KP LUAD model, hyperactivation of oncogenic KRAS/MAPK signaling enables progression from adenoma to adenocarcinoma[31], corresponding with transcriptional divergence from the cell of origin[27,28,30,32]. We reason that this transition may enhance oncogene dependence and sensitivity to pharmacologic inhibition[31,33,34]. Consistent with these results, we found that pERK positivity primarily overlapped with regions of higher grade within vehicle treated tumors (**Fig. 1h**).

Degree of KRAS inhibition modulates alveolar phenotypes in residual disease

While a prior study reported enrichment of an AT1-like signature upon KRAS inhibition[25], our data primarily implicated an AT2 signature (**Fig. 1f, Supplementary Fig. 3d**). To reconcile these results, we considered that the alveolar phenotype observed in RD is dependent on the mechanism of KRAS inhibition. Unlike sotorasib,

the shRNAs used to target *Kras* in the earlier study are not mutant-allele specific. Therefore, we hypothesized that wild-type *Kras* signaling in residual tumors may dictate AT2 vs AT1 differentiation. To test this hypothesis, we initiated tumors in K$_c$P Cas9 mice using lentiviral vectors encoding U6-driven sgRNAs (hU6-sgRNA-EFS-Cre or USEC) targeting either a control locus (sg*Olfr102*), or wild-type *Kras* (sg*Kras*^{WT}) (**Fig. 1i**). We reasoned that knock-out of the wild-type allele would force all *Kras* signaling through oncogenic *Kras*^{G12C}, which we inhibit with sotorasib. After two weeks of sotorasib treatment, USEC-sg*Kras*^{WT} and USEC-sg*Olfr* tumors both demonstrated increased expression of *Hopx*, an AT1 marker, but this effect was comparatively greater in treated USEC-sg*Kras*^{WT} tumors, which exhibited pronounced lepidic histology (**Fig. 1j-k, Supplementary Fig. 4b)**. Interestingly, these tumors retained surfactant (SPC) expression, suggesting that they maintain some AT2 identity (**Supplementary Fig. 4a)**. Collectively, these data demonstrate that drug-tolerant persister cells in our model recapitulate the response observed to MAPK pathway-targeted therapy in human lung adenocarcinoma and support a model in which an alveolar cell transcriptional state is tolerant to KRAS inhibition.

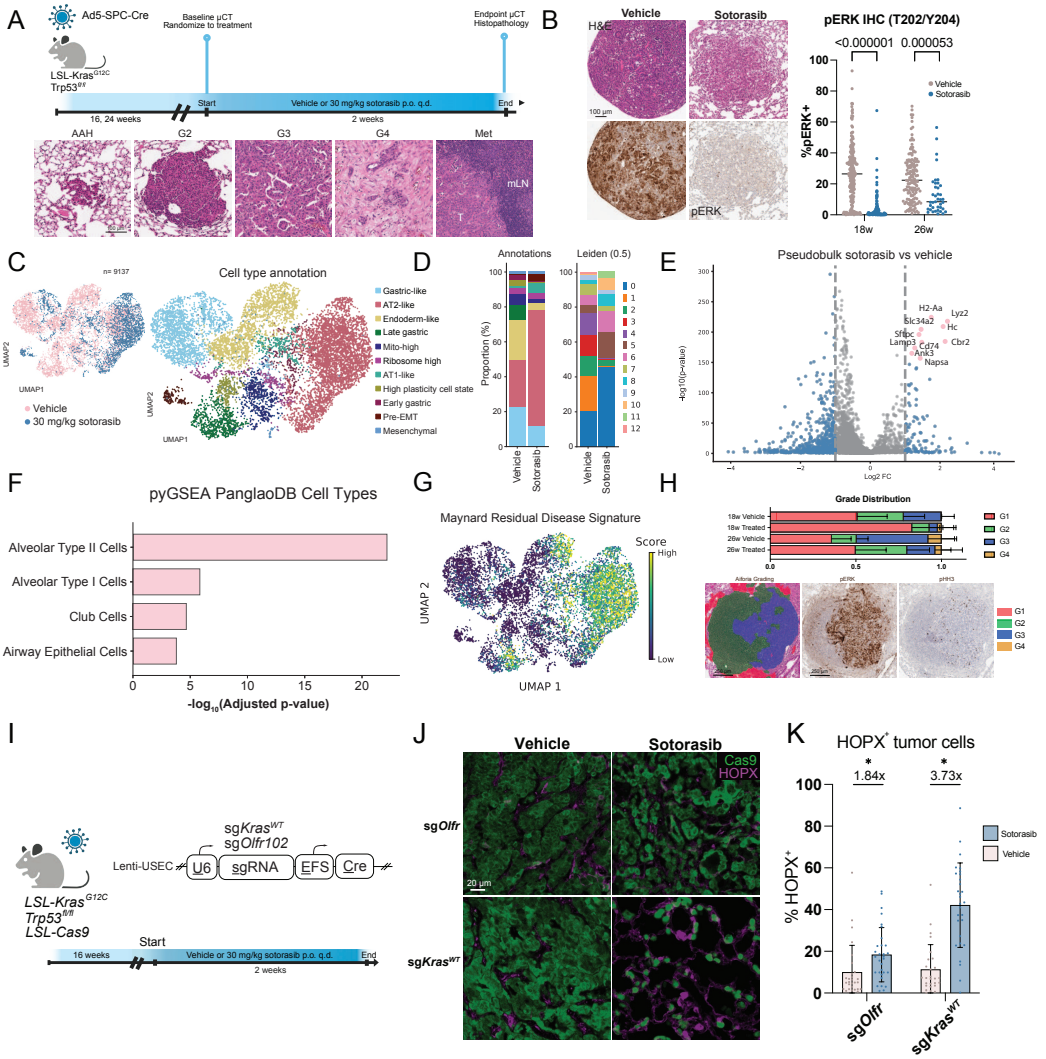


Figure 1. Sotorasib robustly but incompletely causes *Kras^{G12C}* tumor regression

A. Schematic for initiation of autochthonous tumors that span histopathologic progression (below) with drug treatment regimen (above). Scale bar indicates 100 μm.
B. Representative immunohistochemical (IHC) staining of phospho-ERK (pERK T202,Y204) in vehicle and sotorasib treated tumors, with quantification of %pERK$^+$ in 18 (Vehicle: n = 8 mice/n = 202 tumors, Sotorasib: n = 9 mice/n= 99 tumors) and 26 week tumors (Vehicle: n = 7 mice/n = 150 tumors, Sotorasib: n = 8 mice/n= 39 tumors). Scale bar indicates 100 μm. Multiple unpaired t tests were used to determine significance, with q values shown.
C. Projection of 9137 sequenced tumor cells in Uniform Manifold Approximation and Projection for Dimension Reduction (UMAP) space, cells from vehicle treated animals (3) are color-coded in light blue and cells from sotorasib treated animals (3) are color-coded in pink. Results from Leiden unsupervised clustering with a coarseness resolution of 0.5 manually annotated with cell state labels derived from Marjanovic et al. [27] and Yang et al.[28]
D. Distribution of Leiden clusters and cell types annotated from Yang et al.[28] in vehicle and treated animals.
E. Volcano plot of differentially expressed genes from a pseudobulk analysis of differential gene expression across vehicle (left) and sotorasib (right) treated tumor cells. Markers of alveolar type II cell identity are color-coded in pink. A Wilcoxon rank sum test was used to determine p-values.
F. pyGSEA results from pseudobulk differentially upregulated genes in sotorasib treated cells using the PanglaoDB gene set[90].
G. UMAP plot demonstrating projection of residual disease signature from patients treated with targeted EGFR/ALK inhibition onto the mouse Kras^{G12C} dataset. Human residual disease signature from Maynard et al.[29]
H. Aiforia quantification of tumor grade in vehicle and sotorasib treated tumors. G1-2 generally represent adenomas and G3-4 represent invasive adenocarcinoma. Inset: example Aiforia grading of vehicle-treated tumor with corresponding pERK and phospho-Histone H3 (pHH3) IHC to demonstrate MAPK activation, proliferation. (18w n = 9 vehicle, n = 10 sotorasib; 26w n = 9 vehicle, n = 8 sotorasib)
I. Schematic for tumor initiation in LSL-**K**rasG12**C**, Tr**p**53fl/fl, LSL-**Cas9** (**K$_c$P Cas9**) mice using lentiviral vectors (pUSEC) targeting *Olfr102* (neutral locus) or *Kras^{WT}*. 16 weeks post-injection (p.i.), mice were treated for 2 weeks with 30 mg/kg sotorasib.
J. Representative images of immunofluorescence (IF) for HOPX (purple) and Cas9 (green) in vehicle and sotorasib treated tumors from the experiment in **I**. Scale bar indicates 20 μm.
K. Quantification of HOPX$^+$ in Cas9$^+$ tumor cells from the experiment shown in **I**. Multiple unpaired t tests were used to determine significance, asterisk indicates discovery (q value less than 0.05), and fold change is shown below. (**sg*Olfr***: vehicle: n = 28 ROIs from 5 mice, sotorasib: n = 31 ROIs from 5 mice; **sg*Kras^{WT}*** vehicle: n = 27 ROIs from 4 mice, sotorasib: n = 29 ROIs from 4 mice)

Complex structural rearrangements and ecDNAs characterize resistant, *Kras^{G12C}*-amplified tumors

To determine the fate of drug-tolerant disease with sustained KRAS inhibition, we continued to administer daily sotorasib in tumor-bearing K$_c$P Cas9 mice until the emergence of resistant tumors (**Fig. 2a**). 16 weeks after tumor initiation, we treated tumor-bearing (USEC-sg*Olfr*) animals for up to 12 weeks with daily sotorasib. Longitudinal μCT demonstrated that a fraction of tumors initially regressed and then re-emerged after 6-10 weeks of daily treatment, suggesting resistant disease (**Fig. 2a**). In some cases, the extent of resistant tumor burden necessitated early animal euthanasia. After up to 12 weeks of treatment, resistant tumors exhibited glandular histology and were NKX2-1$^+$, consistent with adenocarcinoma, and universally stained positively for

pERK, indicating restoration of MAPK signaling (**Fig. 2b**). To investigate potential genetic mechanisms of resistance, we first performed targeted hybrid capture DNA sequencing of these tumors. We observed no obvious causal point mutations, including no detected secondary *Kras* mutations at codon 12 or switch II residues (**Supplementary Fig. 5a**). Copy number analysis indicated that all resistant tumors (n= 10 tumors) focally amplified the oncogenic $Kras^{G12C}$ allele (**Fig. 2c**). While an increase in copy number of oncogenic *Kras* has been reported in the KP GEMM through gain of chromosome 6[33,35], focal amplifications to this extent have not been reported in untreated tumors[36,37], and mirror KRASi resistance mechanisms reported in human patients[15] and preclinical models[38,39]. To determine if *Kras* amplifications were present in sotorasib-naïve tumors, we performed whole-genome sequencing (WGS) on untreated K_cP tumors from a similar time point (24 weeks p.i.). While 4/6 untreated had an extra copy of chromosome 6, only 1/6 harbored a focal (linear) amplification of $Kras^{G12C}$ (**Fig. 2c)**. Notably, the extent of *Kras* amplification in this tumor was lower (estimated copy number = 6.0) than observed in sotorasib-resistant tumors (CN=11.0-32.24).

To determine the mechanism of $Kras^{G12C}$ amplification, we resequenced resistant tumor DNA by WGS. Using AmpliconArchitect[40], we inferred that $Kras^{G12C}$ amplification in at least 4/10 resistant tumors occurred as $Kras^{G12C}$ extrachromosomal DNAs (ecDNAs) (**Fig. 2d, Supplementary Fig. 5b**). The remainder were delineated 'Complex, non-cyclic' amplifications (**Supplementary Fig. 5c**), and featured considerable rearrangement and intrachromosomal breakpoints. In these non-cyclic amplifications, we observed recurrent (4/10) breakpoints that included *Ksr2* (**Supplementary Fig. 5c**), a pseudokinase that scaffolds Ras-independent dimerization of Raf proteins, perhaps further contributing to insensitivity to KRAS inhibition[41]. In addition to $Kras^{G12C}$, AmpliconArchitect also identified ecDNA amplifications of *Mycn* (n=3, CN 26.85-62.7) and *Myc* (n=1, CN = 5.78) in 4/10 resistant tumors. ecDNAs ranged in size from 0.33 Mb to 2.5 Mb (**Supplementary Fig. 5b**), consistent with ecDNAs previously described in other tumors[42,43]. While c-Myc amplification has been reported as a preclinical resistance mechanism to RAS(ON) therapy in PDAC[44], we are not aware of reports implicating N-Myc in clinical or preclinical KRAS inhibitor resistance. Tumors with Myc amplifications exhibited IHC positivity for N-MYC and c-MYC, respectively, confirming protein expression (**Fig. 2e, Supplementary Fig. 5d**). The significant degree of genomic complexity within these amplifications was notable and may reflect bulk sequencing of a genomically heterogenous population of cells. As we did not perform ultra-deep sequencing of these tumors, we cannot rule out the presence of ecDNAs in resistant tumors with 'Complex-non-cyclic' $Kras^{G12C}$ amplifications. Collectively, we demonstrate that prolonged sotorasib treatment *in vivo* generates resistant adenocarcinomas that genetically restore MAPK signaling. Mechanistically, we identify both complex rearrangements and ecDNAs that amplify $Kras^{G12C}$ as well as Myc paralogs as putative drivers of resistance.

Rb1 deficient resistant tumors do not undergo small cell transformation

Although genetic restoration of KRAS-MAPK signaling has been described as a major driver of KRAS inhibitor resistance in patients, we also sought to model non-genetic mechanisms such as histologic transformation. We first tried to model neuroendocrine transformation by generating *Rb1*-deficient K_cP models by CRISPR-KO (**Supplementary Fig. 6a**). Although RB1 mutations are rare in KRAS mutant human lung cancer, *RB1* deficiency is nearly universally observed in TKI-induced small cell transformation (tSCLC)[12]. K_cP; $Rb1^{KO}$ tumors were highly proliferative, consistent with the role of RB in cell cycle regulation (**Supplementary Fig. 6c**), and aggressive, showing evidence of epithelial to mesenchymal transition and seeding macrometastases to the liver (**Supplementary Fig. 6b**). *Rb1* knock-out did not exhibit primary resistance to KRAS inhibition, however, as tumors exhibited reduced tumor burden after 2 weeks of sotorasib treatment (**Supplementary Fig. 6d**). After 12 weeks of treatment, resistant K_cP;$Rb1^{KO}$ tumors emerged with similar kinetics as controls, but we did not observe small cell transformation. The resistant K_cP;$Rb1^{KO}$ tumors were negative for neuroendocrine (CGRP, UCHL1) and squamous markers (ΔNp63); however, a subset of tumors did exhibit sarcomatoid, spindle-cell (Vimentin$^+$) histology (**Fig. 2F**). Most K_cP;$Rb1^{KO}$ resistant tumors, including the mesenchymal tumors, demonstrated evidence of MAPK reactivation and harbored corresponding (n=5/7) $Kras^{G12C}$ amplifications, as observed in resistant sg*Olfr* tumors (**Supplementary Fig. 6e)**. Interestingly, tumors that did not amplify $Kras^{G12C}$ were pERK negative, suggesting engagement of alternative oncogenic signaling pathways (**Supplementary Fig. 6f)**. Notably, tSCLC transitions have not yet been described in patients treated with KRAS inhibitors, and despite sustained KRAS inhibition, we were not able to model SCLC transformation with *Rb1* loss.

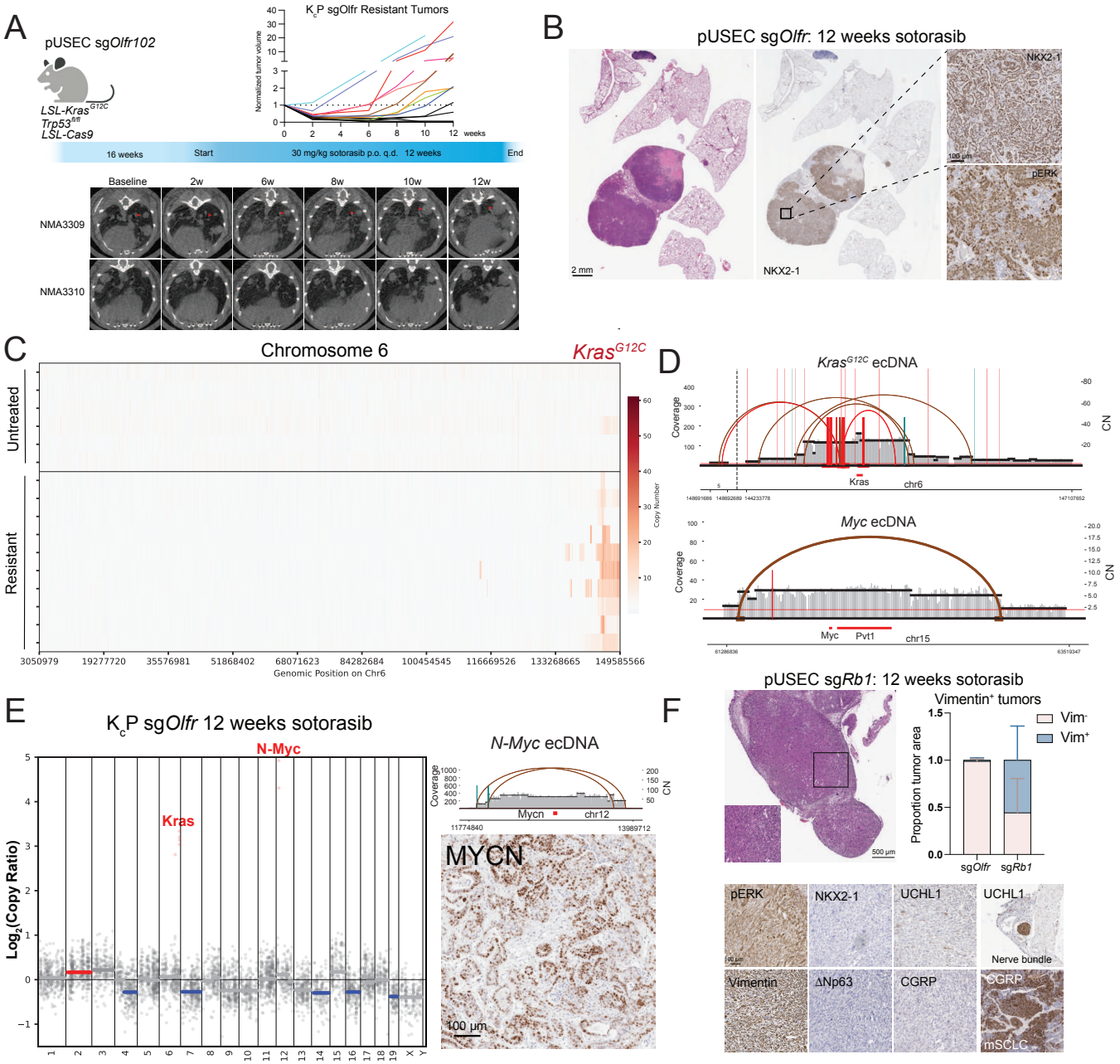


Figure 2. Resistance emerges *in vivo* with sustained sotorasib treatment

A. Schematic for initiation and 12-week sotorasib treatment of autochthonous tumors in K$_c$P Cas9 mice with USEC-sg*Olfr*. Below: representative series of μCT frames demonstrating initial regression and relapse of an sg*Olfr102* tumor over 12 weeks of daily sotorasib treatment. Above: Spider plot for tumor volumes, quantified from μCT data, in K$_c$P Cas9 sg*Olfr* mice starting 16w p.i. with daily sotorasib treatment for up to 12 weeks. Tumor volumes were normalized to initial volume. N= 14 tumors were quantified from n= 3 mice. Note: data were not collected at 4 weeks after treatment initiation.

B. H&E stain with serial immunohistochemistry on a resistant K$_c$P-sg*Olfr* tumor following 12 weeks of sotorasib treatment. NKX2-1 immunohistochemistry was used to confirm adenocarcinoma histology. Insets demonstrate NKX2-1 positive nuclei, as well as positivity for phosphorylated

ERK (pERK), demonstrating MAPK reactivation. Scale bars indicate 2 mm, 100μm where indicated.

C. Copy number profiles for chromosome 6 determined indicating focal amplification of *Kras*^{G12C} in K_cP tumors. Copy number profiles called using CNVkit and plotted using .cnr files. n = 6 untreated tumors shown (24 weeks p.i.) and n= 10 resistant tumors (26 weeks p.i.)
D. Structural Variant views for *Kras*^{G12C} and *Myc* ecDNAs from a resistant tumor, demonstrating copy number and ecDNA breakpoints.
E. Left: Resistant tumor targeted sequencing CNV analysis demonstrating log2(copy number ratios) of loci across the mouse genome. CNVkit was used to call significant copy number alterations which are colored in red for gains and blue for losses. Gene names for *Kras* and *Mycn* were manually included after determining the genes associated with the called focal amplification. Right: AmpliconArchitect plot structural variant (SV) view demonstrating breakpoints and copy number for *Mycn* ecDNA. Below: MYCN IHC in the corresponding tumor, scale bar indicates 100 μm.
F. H&E and IHC for a representative *Rb1*^{KO} resistant tumor after 12 weeks of sotorasib treatment. IHC includes markers for adenocarcinoma (NKX2-1), mesenchymal tumors (Vimentin), squamous tumors (ΔNp63), neuroendocrine tumors (UCHL1, CGRP), and MAPK signaling (pERK). Positive controls from murine small cell lung cancer (mSCLC) and a nerve bundle are used for CGRP and UCHL1, respectively. Below: Quantification of Vimentin$^+$ tumors in sg*Olfr* resistant tumors and *Rb1*^{KO} resistant tumors (n = 6 sg*Olfr*, n = 6 sg*Rb1*).

Human scRNA sequencing nominates transcription factors driving adenosquamous transitions

Unlike neuroendocrine transformation, adeno-to-squamous histologic transformations have been documented in patients treated with adagrasib[15,18]. These occur independent of evident secondary driver mutations, suggesting epigenetic reprogramming. To model squamous transformation in the setting of KRAS inhibition, we first considered putative transcription factor drivers of the adeno-to-squamous transformation. We analyzed previously published tumor scRNA sequencing from a patient with EGFR$^{\Delta 746\text{-}750}$ mutant adenocarcinoma that underwent squamous transformation on the EGFR inhibitor osimertinib[29] (**Fig. 3a**). While limited to 226 cancer cells between treatment naïve (TN), residual disease (RD) and progression and histologic transformation (PD), we observed expected gene expression changes in cells from PD samples. These included decreased *NKX2-1* and *SFTPC* expression, consistent with loss of alveolar identity, and upregulation of keratin genes (*KRT5*, *KRT14*, *KRT16*) (**Supplementary Fig. 7a, Supplementary Table 6**). To identify transcription factors associated with a shift to a squamous cell state, we used Chea3[45] on the top differentially expressed genes identified by pseudobulk analysis comparing PD to TN/RD, curating a list of candidate transcription factors that might drive the squamous phenotype (**Fig. 3a, Supplementary Table 6**). While limited by a relatively small number of cells, all of the top candidate transcription factors identified (*GRHL3,TP63, ZNF750, SOX15, HES2, IRX4*) are more highly expressed in human lung squamous carcinoma than adenocarcinoma, supporting the utility of this analysis (**Fig. 3b**).

ΔNp63 expression *in vitro* facilitates squamous reprogramming, *Kras* independence

To evaluate if candidate transcription factor expression is sufficient for squamous transformation and KRAS inhibitor resistance, we generated alveolar organoids from *LSL-Kras^{G12D},Trp53$^{fl/fl}$;R26:LSL-dCas9 VPR* (KP-VPR) mice. These organoids harbor a Cre-conditional CRISPR activation (CRISPRa) allele that enables over-expression of endogenous targeted genes[46]. We infected KP-VPR organoids with USEC vectors encoding sgRNAs targeting the promoters of each candidate transcription factor (*Grhl3,Trp63, Zfp750, Sox15, Hes2, Irx4*) (**Fig. 3c**), confirming target activation by RT-qPCR (**Supplementary Fig. 7b**). Treatment with MRTX1133, an allele-specific KRAS^{G12D} inhibitor[47], inhibited growth across these organoids, as measured by Incucyte live cell imaging, with the exception of those expressing sg*Trp63*, which activates the ΔN isoform of p63 (hereby sg*ΔNp63*), a master transcription factor in keratinizing epithelia[48–51] (**Fig. 3c**).

In addition to resistance to KRAS inhibition, KP-sg*ΔNp63* organoids adopted a comparatively solid morphology (**Fig. 3c**) and demonstrated increased expression of squamous genes at the RNA (*Krt5, Krt14, Krt6a, Dsc3*) (**Fig. 3d**) and protein level (KRT5, SOX2) (**Fig. 3f**). MRTX1133 treatment caused minimal change in pERK and no induction of apoptosis in KP-sg*ΔNp63* organoids (**Fig. 3e**), confirming insensitivity to KRAS inhibition. Interestingly, KP-sg*ΔNp63* organoids demonstrated minimally detectable protein expression of oncogenic KRAS^{G12D} (**Fig. 3f**). By RT-qPCR, we identified decreased *Kras* mRNA abundance, and only 10% of *Kras* transcript reads corresponded to oncogenic *Kras^{G12D}* (**Supplementary Fig. 7c**). This may reflect selection against clones with oncogenic *Kras* expression and may explain insensitivity to KRAS inhibition. In human LUSC cell lines, *TP63* transcript levels correlate with the HALLMARK_KRAS_Signaling_DOWN Gene Set (**Supplementary Fig. 7d)**, consistent with our organoid results. Collectively, activation of ΔNp63 expression renders KP organoids insensitive to KRAS inhibition, is associated with decreased *Kras* expression, and induces several squamous-associated genes.

ΔNp63 expressing squamous organoids form squamous tumors *in vivo*

To evaluate if KP-sg*ΔNp63* organoids were tumorigenic, we orthotopically transplanted KP-sg*ΔNp63* and control KP-sg*Olfr* organoids into LSL-VPR syngeneic recipient mice. 10 weeks after transplantation, recipients of either organoid line exhibited considerable tumor burden (**Supplementary Fig. 8a**). We observed exclusively advanced adenocarcinoma in KP-sg*Olfr* recipients, but KP-sg*ΔNp63* recipient animals harbored both adenocarcinomas as well as squamous cell carcinomas (**Fig. 3g**). We repeated this experiment with KP-sg*ΔNp63* organoids from later passages, which more homogeneously exhibited solid, squamous-like morphology, and these nearly universally generated squamous tumors (**Fig 3g**). Expectedly, KP-sg*ΔNp63* squamous tumors were ΔNp63^{+} and NKX2-1^{-} (**Fig. 3h, Supplementary Fig. 8b**), whereas KP-sg*ΔNp63* adenocarcinomas were ΔNp63^{-} and NKX2-1^{+}, perhaps indicating silencing or downregulation of the sgRNA. We observed significantly lower pERK positivity in squamous tumors (**Fig. 3i**), supporting a model wherein squamous tumors are intrinsically less dependent on KRAS/MAPK signaling. Other groups have implicated

MYC, AKT and STAT3 signaling in squamous transformed tumors[52,53]. We observed robust pSTAT3 nuclear staining in squamous tumors, but also in adenocarcinomas, suggesting this signaling axis may not be specific to squamous histology (**Supplementary Fig. 8c**). In either histologic subtype we observed minimal pAKT staining and no striking differences in MYC expression by immunohistochemistry **(Supplementary Fig. 8c)**. Taken together, orthotopic transplantation of KP organoids overexpressing ΔNp63 was sufficient to generate squamous tumors with lower levels of activity in the MAPK pathway, implicating ΔNp63 as a master regulator of squamous identity and, potentially, *Kras* independence

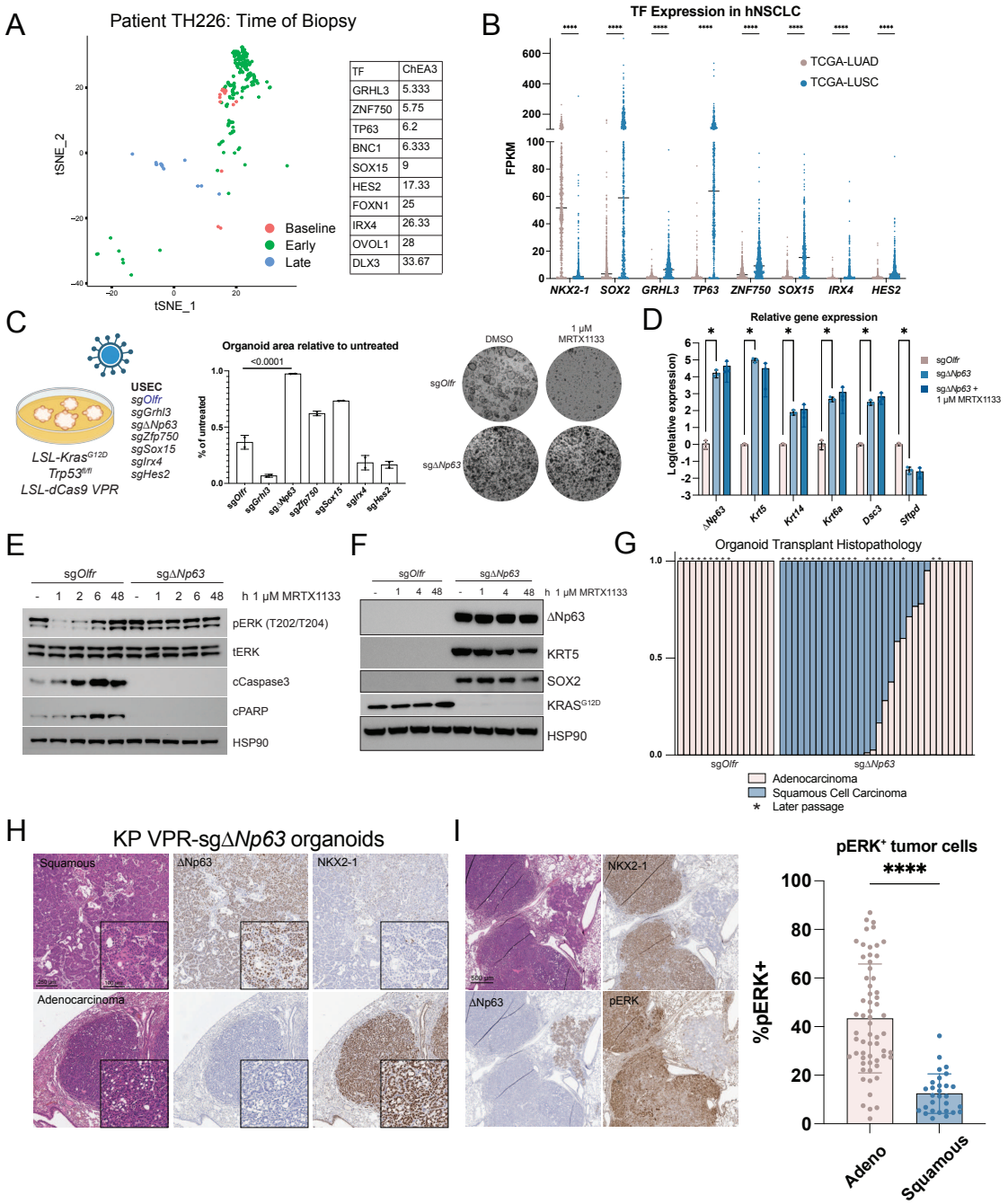


Figure 3. ΔNp63 drives squamous reprogramming, KRAS inhibitor resistance in alveolar KP organoids.

A. Left: t-SNE plots from a human EGFR exon 19 deletion-mutant NSCLC tumor treated with osimertinib either pretreatment (Baseline), at maximal tumor regression (Early), or after histologic transformation and relapse as squamous cell carcinoma (Late). Right: Chea3 output on transcription factors predicted to drive the expression of the top differentially expressed genes from a pseudobulk analysis comparing Late to Early/Baseline tumor cells.
B. Transcripts per million (TPM) comparing expression of candidate transcription factors between patients with lung adenocarcinoma (n = 500 patients, TCGA-LUAD, pink) to squamous cell carcinoma (n = 494 patients, TCGA-LUSC, blue). NKX2-1 expression used as a positive control for adenocarcinoma.
C. Left: Incucyte organoid growth for KP-VPR organoids infected with USEC vectors (n = 2 replicates) targeting the promoters of candidate transcription factors after 192 hours in MRTX1133, normalized to growth in DMSO. Right: Microscopy images of KP-sg*Olfr* and KP-sg*ΔNp63* organoids grown in MRTX1133 or DMSO after 192 hours.
D. RT qPCR quantification of relative gene expression of several squamous-associated genes (*ΔNp63* - targeted by CRISPRa, *Krt5, Krt14, Krt6a, Dsc3*) as well as alveolar genes (*Sftpd*), normalized to *Gapdh* expression. (n = 3 technical replicates used).
E. Immunoblotting for MAPK signaling (pERK, tERK) and markers of apoptosis (Cleaved Caspase 3, cleaved PARP) upon timecourse KRAS inhibition. DMSO used as a control. HSP90 used as a loading control.
F. Immunoblotting for squamous markers (ΔNp63, KRT5, SOX2), and oncogenic *Kras* expression ($KRAS^{G12D}$) in KP-sg*Olfr* and KP-sg*ΔNp63* organoids in a timecourse MRTX1133 experiment. HSP90 used as a loading control.
G. Spectrum of tumor histopathology from KP-VPR organoid transplant experiments 10 weeks after orthotopic transplantation. Left: KP-VPR sg*Olfr* (n = 16), Right: KP-sg*ΔNp63* (n=32). Asterix (late) indicates passages 7-10, lack of asterix (early) indicates passage 5. Squamous histology was called by a combination of H&E review and ΔNp63 positivity.
H. H&E and IHC from orthotopic KP-sg*ΔNp63* recipients. IHC for NKX2-1 and ΔNp63 as markers of adenocarcinoma and squamous cell carcinoma, respectively
I. pERK IHC and quantification in adenocarcinomas and squamous cell carcinomas emerging from KP-sg*ΔNp63* organoid orthotopic transplant. n= 29 squamous tumors and n= 61 adenocarcinomas were used for quantification. An unpaired t test was used to determine significance. **** indicates $p<0.0001$.

ΔNp63 overexpression in autochthonous tumors is insufficient for squamous transformation and suppresses *Kras*-mediated tumorigenesis

To evaluate if ΔNp63 expression is sufficient for autochthonous squamous transformation and KRAS inhibitor resistance, we infected K_CP, LSL-dCas9 VPR animals with the same pUSEC vectors targeting *ΔNp63* and *Olfr*. Surprisingly, tumor burden was significantly decreased in USEC-sg*ΔNp63* mice compared to USEC-sg*Olfr* 18 weeks after initiation (**Fig. 4a**). By immunohistochemistry, we could identify small, weakly $\Delta Np63^{+}$ lesions in a subset of mice, confirming CRISPR activation (**Supplementary Fig. 9a**). These tumors resembled early adenomatous hyperplasias and did not exhibit squamous differentiation. To ensure that decreased tumor burden was not an artifact of dCas9-VPR activation of the upstream promoter of the TAp63 isoform, which functions as a tumor suppressor[54,55], we engineered a lentiviral vector with a ΔNp63α cDNA coupled to Cre expression (lenti-ΔNp63-Cre) (**Supplemental Fig.**

9b). Similarly, lenti-ΔNp63-Cre tumors were nonsquamous and generally ΔNp63$^-$ or weakly ΔNp63$^+$, possibly due to downregulation of the expression vector (**Supplementary Fig. 9c**). Despite limited tumor burden, we treated both VPR (n = 11) and cDNA models (n = 10) (16 weeks p.i.) for up to 10 weeks of sotorasib, but did not observe primary resistance or the emergence of squamous tumors (**Fig. 4e, h**). These findings demonstrate that ΔNp63 alone is insufficient *in vivo* to drive squamous transformation and suppresses *Kras*-driven tumorigenesis in this model system.

K_cP tumors and human LUADs express SOX2, which is not sufficient for the squamous phenotype

As ectopic ΔNp63 expression was insufficient to reprogram K_cP tumors to squamous identity, we considered the possibility that increased lineage plasticity might be a prerequisite for squamous transformation. In *Lkb1*-deficient models shown to undergo adenosquamous transitions[18–20,56], Ji and colleagues identify *Krt6a* as a biomarker for this plastic cell state[18]. Notably, *Krt6a* is the top gene induced in KP tumors engineered to overexpress the airway transcription factor *Sox2*[57]. Extensive work has shown that *Sox2* expression increases lineage plasticity and cooperates with ΔNp63 in driving squamous fate[57,58], and we hypothesized that ectopic *Sox2* expression may enable tumors to undergo drug-induced squamous transformation. Unlike ΔNp63, we detected SOX2 in some K_cP tumors, suggesting that expression is compatible with tumorigenesis (**Supplementary Fig. 9d**). We corroborated this in human NSCLC, observing that ΔNp63 is exclusively expressed in LUSC, but SOX2 expression is detectable in both LUAD and LUSC (**Fig. 4b**). Bulk RNA sequencing of isogenic KP-VPR lines infected with USEC sg*Olfr*, sg*ΔNp63*, sgSox2, and sg*ΔNp63*-sg*Sox2* demonstrated that unlike *ΔNp63*, *Sox2* expression alone did not induce squamous transcriptional signatures (**Fig. 4c, Supplementary Table 7**). However, *Sox2* expression was associated with increased chromatin accessibility at loci unique to squamous organoids, corresponding with ΔNp63 consensus motifs, perhaps indicating induction of an intermediate epigenomic cell state (**Fig. 4d**).

Sox2 expression in autochthonous tumors is tolerated through *Kras*-mediated tumorigenesis and can enable drug-induced histologic transformation

To evaluate the role of *Sox2* in lineage plasticity, we generated VPR-based (USEC sg*Sox2*) and cDNA (lenti-*Sox2*-Cre) K_cP models to overexpress *Sox2* in autochthonous K_cP tumors (collectively, K_cP-*Sox2*^{OE}). Unlike our experience with ectopic ΔNp63 expression, we did not observe significant suppression of tumor burden in this model (**Fig. 4a)**. Consistent with previous literature[59], untreated K_cP-*Sox2*^{OE} tumors exclusively formed adenocarcinomas, with no baseline squamous histology. As reported[57], SOX2 positivity corresponded with reduced NKX2-1 expression *in vitro* and *in vivo*, suggesting that SOX2 may suppress alveolar identity (**Supplementary Fig. 10a,b**).

To characterize response and resistance to KRAS inhibition, we treated K_cP-*Sox2*^{OE} models (16 weeks p.i.) with daily sotorasib for 2 and 10 weeks. We observed significant

tumor regression within two weeks, indicating a lack of primary resistance to KRAS inhibition. After 10 weeks of sotorasib treatment, we observed the emergence of resistant tumors with similar kinetics as our prior experiments (**Fig. 4e**). Resistant SOX2$^+$ tumors exhibited considerable histologic diversity, including NKX2-1$^-$ papillary adenocarcinomas, poorly differentiated tumors, as well as squamous tumors in a small fraction of both K_cP VPR sg*Sox2* (4%, n = 1/27) and K_cP lenti-*Sox2* mice (6%, n=1/18) treated for 10 weeks with sotorasib (**Fig. 4e,h, Supplementary Fig. 10c**). These rare, SOX2$^+$ squamous-transformed tumors were ΔNp63$^+$ and KRT5$^+$ (**Fig. 4e**), providing further evidence that ΔNp63 expression is a defining feature of squamous histology. Resistant NKX2-1$^-$, SOX2$^+$ non-squamous tumors, mostly papillary adenocarcinomas, were ΔNp63$^-$ and pERK$^+$, suggesting reactivation of MAPK signaling (**Supplementary Fig. 10c**). Consistent with our earlier findings, we detected *Kras*^{G12C} amplifications in two of these tumors analyzed by WGS.

To reconcile the rare incidence of squamous transformation in the setting of SOX2 overexpression, we considered that cells with the capacity for histologic transformation may emerge from a cell of origin that is poorly initiated by USEC. We noted that a squamous transformed tumor we observed in the K_cP-VPR *Sox2* model was immediately adjacent to an airway. *Scgb1a1*$^+$ airway cells (generally club cells) have been demonstrated as the cell of origin in *Kras* plus *Lkb1* mutant adenosquamous tumors[56,60]. In addition, these cells are maintained by basal stem cell pools, and have the capacity to transdifferentiate towards a basal phenotype in the context of injury and tumorigenesis[61–63]. We therefore initiated K_cP VPR mice with a modified USEC vector with a CCSP (*Scgb1a1*) promoter driving Cre expression and either sg*Sox2* or sg*Inert*, presumably favoring transformation of airway cells (U6-sgRNA-CC10-Cre or USCC) (**Fig. 4f**). After 18 weeks following tumor initiation, we observed USCC-initiated tumors primarily adjacent to small bronchioles (**Supplementary Fig. 10d**). Although USCC-sg*Sox2* tumors were non-squamous, they exhibited robust SOX2 expression, variable suppression of NKX2-1, as well as isolated ΔNp63$^+$ cells (**Supplementary Fig. 10d,e**). We treated both USCC-sg*Inert* and USCC-sg*Sox2* mice for 10 weeks with daily sotorasib. While we exclusively observed resistant adenocarcinoma in USCC-sg*Inert* mice (n = 10), 1/5 (20%) of USCC-sg*Sox2* mice had squamous histology at time of resistance (**Fig. 4g,h**).

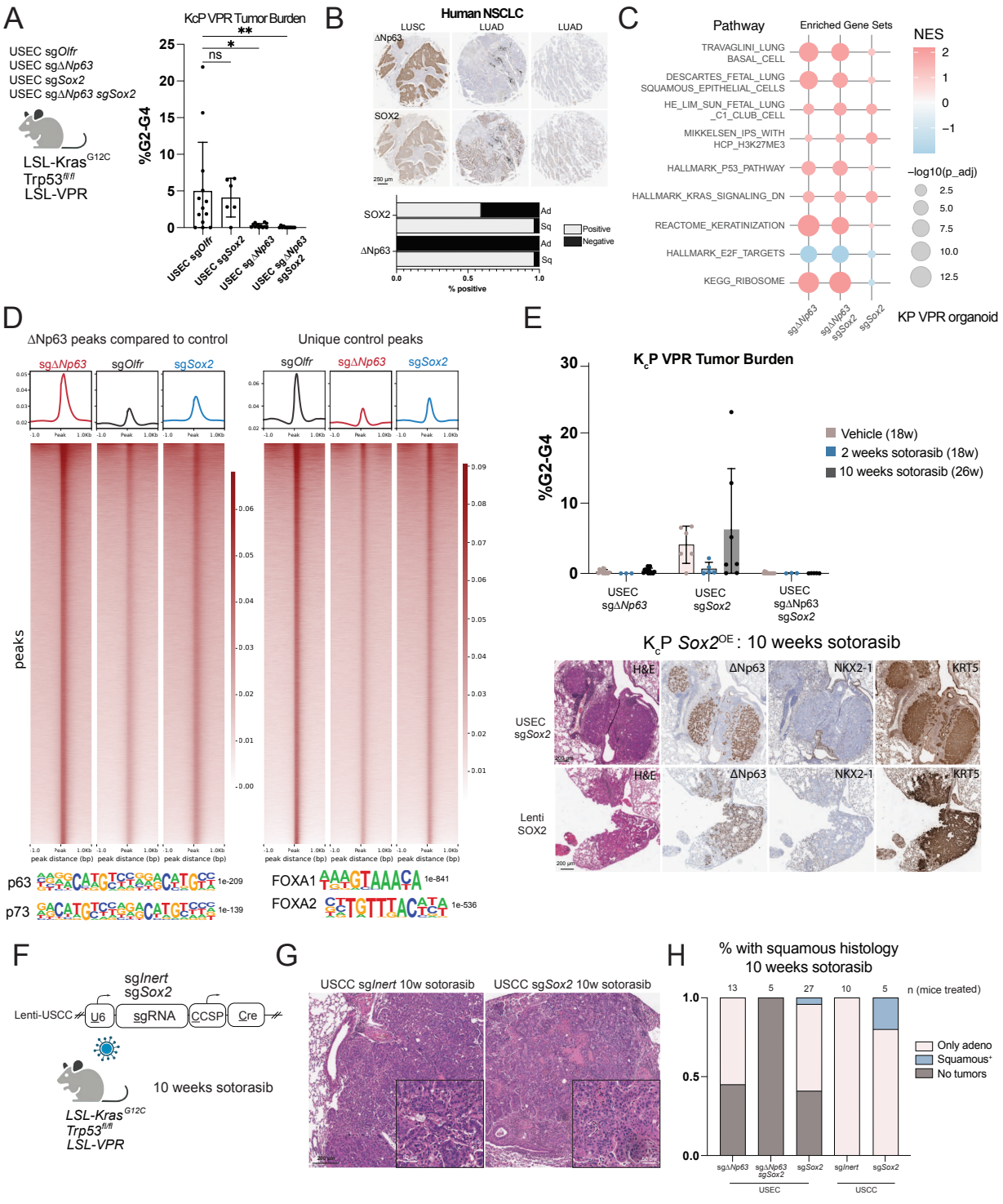


Figure 4. Sox2 enables histologic transformation in autochthonous models of adenosquamous transition

A. Schematic for autochthonous models of ΔNp63 overexpression. K$_c$P VPR mice were infected with USEC vectors targeting *Olfr102*, *ΔNp63, Sox2*, or a dual *ΔNp63/Sox2* vector. Right: quantification of tumor burden (G2-G4) from K$_c$P VPR mice 18 weeks p.i. (n = 13 sg*Olfr*, n = 6 sg*Sox2*, n = 12 sg*ΔNp63*, n = 12 sg*ΔNp63* sg*Sox2*)

B. Representative tissue microarray (TMA) IHC ΔNp63 and SOX2 in human NSCLC. Quantification indicates the proportion of cores that are ΔNp63 and SOX2 positive, respectively (n = 22 adenocarcinoma, n = 28 squamous cell carcinoma)
C. Gene set enrichment analysis performed on KP-VPR organoids comparing sg*ΔNp63*, sg*Sox2*, and a dual sg*ΔNp63*-sg*Sox2* vector to sg*Olfr* control organoids.
D. Chromatin accessibility at MACS2 narrow_peaks called from bulk organoid ATAC sequencing. Left: accessibility across conditions at peaks that distinguish sg*ΔNp63* organoids from control organoids. Bottom left: HOMER motif analysis on shared peaks between sg*Sox2* and sg*ΔNp63* organoids that are not called in sg*Olfr* organoids. Right: accessibility across conditions at peaks that distinguish sg*Olfr* organoids from sg*Sox2* and sg*ΔNp63* organoids. Bottom right: HOMER motif analysis on peaks unique to sg*Olfr*.
E. Top: quantification of tumor burden (G2-G4) from K_cP VPR mice 18 or 26 weeks (10 weeks sotorasib). Vehicle mice are the same as those shown in Fig. 4a (n = 6 sg*Sox2*, n = 12 sg*ΔNp63*, n = 12 sg*ΔNp63* sg*Sox2*). 2 weeks treatment (n = 3 sg*Sox2*, n = 5 sg*ΔNp63*, n = 3 sg*ΔNp63* sg*Sox2*). 10 weeks treatment (n = 23 sg*Sox2*, n = 13 sg*ΔNp63*, n = 5 sg*ΔNp63* sg*Sox2*). Bottom: H&E and IHC for squamous transformed tumors in $Sox2^{OE}$ models treated for 10 weeks with sotorasib. Scale bar indicates 200 μm.
F. Schematic for tumor initiation with U6-sgRNA-CCSP-Cre (USCC) in K_cP VPR mice. Mice began treatment 16 weeks p.i. and received daily 30 mg/kg sotorasib for 10 weeks.
G. H&E staining for transformed squamous USCC-sg*Sox2* tumor and a resistant USCC-sg*Inert* adenocarcinoma after 10 weeks of sotorasib. Scale bar indicates 200 μm and 50 μm in the insert.
H. Proportion of mice exhibiting resistant tumor burden and squamous transformation after 10 weeks of sotorasib.

Genetic loss of *Nkx2-1* promotes mucinous tumorigenesis, accelerates squamous transformation

In GEMMs of primary squamous cell carcinoma, genetic inactivation of *Nkx2-1* dramatically accelerates squamous tumorigenesis even in models where Sox2 suppresses alveolar identity[59]. Although seldom genetically lost in human lung cancer, *Nkx2*-1 enforces AT1/AT2 identity[64] and constrains gastric/squamous gene expression[57,58,65]. We therefore targeted *Nkx2-1* by CRISPR-KO to perform short and long-term sotorasib treatment experiments (**Fig. 5a**). Upon tumor initiation, *Nkx2-1* knockout produced considerable histologic diversity, including mucinous tumors characterized by columnar epithelial cells, mucin production, and loss of alveolar marker expression (**Fig. 5a, Supplementary Fig. 11a,e)**. Mucinous tumors were strongly positive for pERK relative to non-mucinous tumors. Similarly, *Nkx2-1* mutation in K_cP alveolar organoids corresponded with an increase in pERK by immunoblotting, suggesting that *Nkx2-1* restrains downstream MAPK signaling (**Supplementary Fig. 11a-b**).

In short-term treatment experiments, we observed a distinct decrease in the fraction of mucinous histology in residual sg*Nkx2-1* tumors (**Supplementary Fig. 11g**). This was notable as mucinous histology has been reported as a putative resistance mechanism to KRASi in *Kras^{G12C};Lkb1* mutant models[19,66]. Based on the strong pERK intensity of mucinous tumors, as well as their pronounced sensitivity to sotorasib, we speculate that mucinous tumors generated by *Nkx2-1* loss are hyperdependent on KRAS/MAPK signaling. To confirm that lack of mucin was not simply due to anabolic suppression

from KRAS inhibition, we compared K_cP sg*Nkx2-1* animals treated for three weeks of vehicle or sotorasib to animals treated with two weeks of sotorasib followed by a one-week drug holiday (**Supplementary Fig. 11d**). While the proliferative index of holiday-treated tumors recovered and exceeded vehicle treated tumors (**Supplementary Fig. 11f**), we observed a persistent reduction in mucinous histology (**Supplementary Fig. 11g**), suggesting that this cell state is highly sensitive to KRAS inhibition.

With long-term *in vivo* sotorasib treatment (12 weeks), 33% (4/12) of USEC-sg*Nkx2-1* mice had evidence of resistant tumors with squamous histology (**Fig. 5d, Supplementary Fig. 12a**). Untreated *Nkx2-1*^{KO} tumors showed no evidence of squamous differentiation, suggesting that squamous transformation occurred in response to KRAS inhibition. These tumors exhibited distinguishing hallmarks of squamous cell carcinoma: abundant eosinophilic cytoplasm, intercellular bridges, keratinization, and infiltration by neutrophils. By immunohistochemistry, transformed squamous (tSCC) tumors were non-mucinous, NKX2-1^{-}, ΔNp63^{+}, FOXA1^{+}, FOXA2^{-}, and variably SOX2^{+} (**Fig. 5c, Supplementary Fig. 12a**).

Combined Nkx2-1 loss and Sox2 expression cooperate to produce adenosquamous histology

As both *Nkx2-1*^{KO} and *Sox2*^{OE} were sufficient to mediate squamous transformation at some frequency following sotorasib treatment, we next investigated the combined effects of *Nkx2-1* loss and ectopic *Sox2* expression. To this end, we generated modified USEC-sg*Nkx2-1* vectors encoding cDNAs for SOX2 (**U**6-sg**N**kx2-1-**E**FS-**S**ox2-Cre or UNES) and ΔNp63α (**U**6-sg**N**kx2-1-**E**FS-ΔN**p**63α-Cre or UNEP) (**Supplementary Fig. 9b**). Interestingly, we observed baseline adenosquamous histology in 28% (n = 2/7) of untreated UNES-infected mice, in contrast to none in the SOX2^{OE} or *Nkx2-1*^{KO} models (**Supplementary Fig. 12b**). After 10-12 weeks of sotorasib treatment, resistant squamous tumors were detectable in 3/12 (25%) of UNES mice, similar to but not exceeding the rate (4/12) of squamous transformation in USEC-sg*Nkx2-1*-infected animals. No baseline adenosquamous histology was observed in UNEP-infected mice, although we did observe a squamous transformed tumor in an animal (n=1/9) treated for 10 weeks with sotorasib. These data suggest that *Sox2* expression cooperates with *Nkx2-1* loss to promote squamous lineage commitment, but renders lineage transformation independent of KRAS inhibition.

Squamous transformed tumors exhibit minimal MAPK activity and do not amplify oncogene *Kras*^{G12C}

Consistent with squamous tumors generated by organoid transplantation, autochthonous tSCC tumors were universally pERK negative, suggestive of MAPK independence (**Fig. 5e**). To rule out the possibility of genetic drivers of squamous transformation, we performed WGS on four *Nkx2*-1^{KO} tSCC tumors. We observed no focal *Kras*^{G12C} or *Myc* amplifications, and no other recurrent copy number alterations (**Fig. 5f**). Of note, one tumor harbored a low level amplification of *Yap1*, which has been

implicated in tolerance to KRAS inhibition[67–69], but has unclear roles in squamous tumorigenesis[70] (**Supplementary Fig. 12c**). Active YAP1 protein expression was not obviously increased in this tumor relative to an adjacent resistant adenocarcinoma (**Supplementary Fig. 12d)**. Collectively, we identify the alveolar transcription factor *Nkx2-1* as a barrier to adeno-to-squamous transformation in Kras-driven tumors. These tSCCs lack histologic evidence of MAPK dependence and do not amplify oncogenic *Kras*^{G12C}, supporting an overall model wherein genetic MAPK restoration and lineage transformation engage fundamentally distinct mechanisms of resistance (**Fig. 5g**).

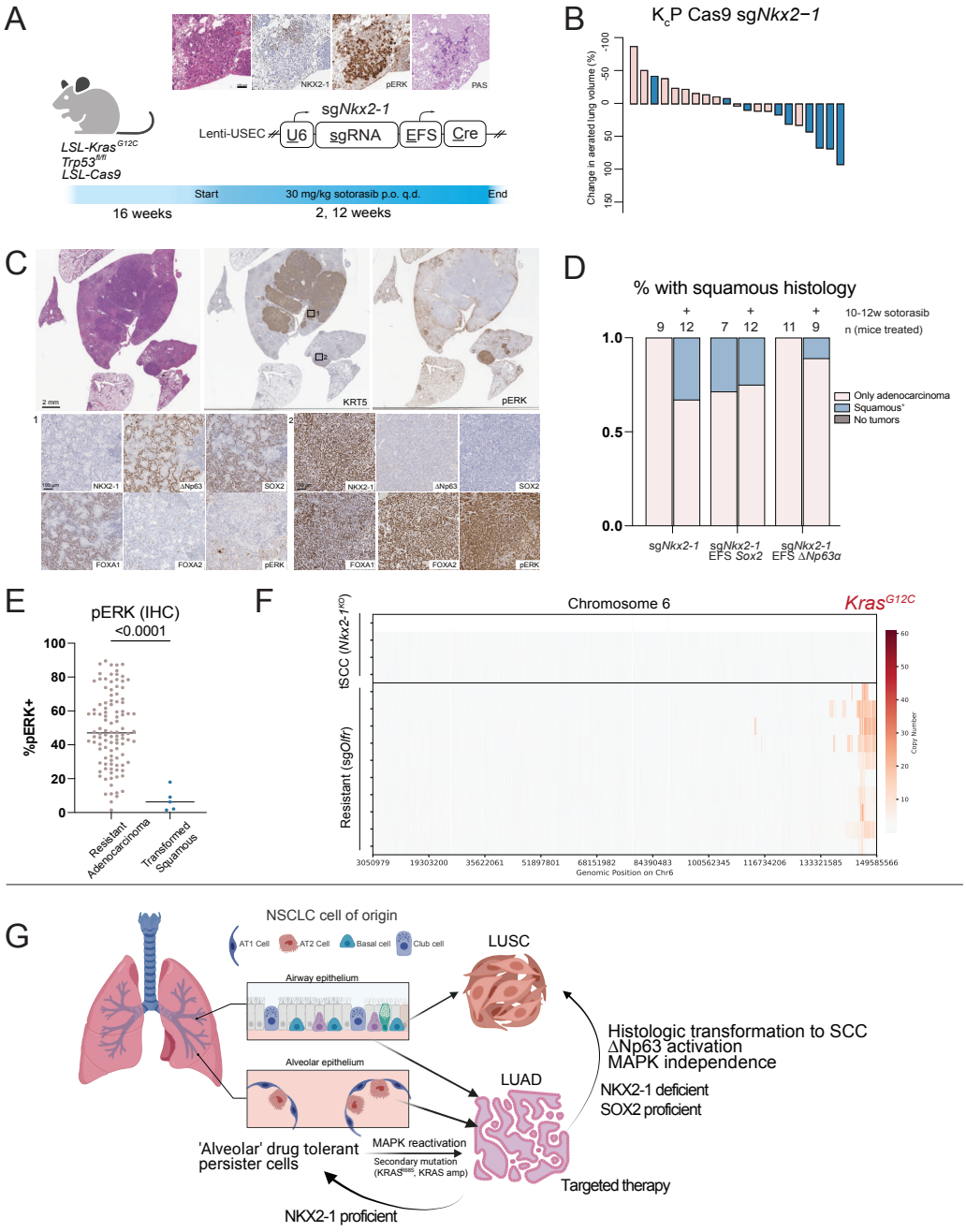


Figure 5. Loss of *Nkx2-1* facilitates squamous transformation and resistance independent of MAPK reactivation

A. Schematic for lentiviral initiation with pUSEC vectors targeting sgRNAs to *Nkx2-1* for CRISPR-KO and subsequently treated for 2 or 12 weeks with daily sotorasib. Histology was taken at the endpoint, and mice were serially monitored by μCT. Above: NKX2-1 and pERK IHC with corresponding Alcian Blue/Periodic Acid Schiff stain for mucin.
B. Waterfall plot of 2-week change in aerated lung volume as calculated by micro-computed tomography (μCT) for USEC-sg*Nkx2-1* (n = 12 vehicle, n = 9 sotorasib) initiated mice treated 16 weeks p.i. As shown in SFig1., the axes are flipped for consistency with waterfall plots from clinical studies.
C. H&E and histopathology of drug resistant squamous transformed tumor in an sg*Nkx2-1*-infected mouse treated for 12 weeks with daily sotorasib. Immunohistochemistry for lineage makers NKX2-1 KRT5, ΔNp63, SOX2, FOXA1, FOXA2, and pERK in both the squamous transformed tumor as well as an adjacent resistant NKX2-1$^+$ adenocarcinoma that arose in the same animal. Scale bars as indicated.
D. Proportion of mice exhibiting resistant tumor burden and squamous transformation after 10-12 weeks of sotorasib.
E. Quantification of pERK IHC in resistant adenocarcinomas (n = 106) and transformed squamous tumors (n = 5) after 10-12 weeks of sotorasib. A two-sided t test is used to determine significance.
F. Copy number profiles for chromosome 6 determined indicating focal amplification of *Kras^{G12C}* in K_cP sg*Olfr* resistant tumors (as shown in Fig. 2c) as well as K_cP sg*Nkx2-1* resistant tumors after 10-12 weeks of sotorasib. Copy number profiles called using CNVkit and plotted using .cnr files. n= 10 resistant tumors (26-28 weeks p.i.) and n = 4 transformed squamous tumors shown (26-28 weeks p.i.).
G. Model for emergence of diverse mechanisms of resistance to targeted therapy, as they pertain to cell lineage.

Discussion:

Our work uncovers diverse mechanisms of resistance to KRAS inhibition in preclinical mouse models of lung cancer. Upon acute KRAS inhibition, we observed that drug tolerant tumor cells resemble differentiated alveolar epithelial cells. We found that the degree of KRAS suppression modulates the phenotype of drug-tolerant residual disease. In tumors with an intact wild-type *Kras* allele, residual tumor burden exhibited an AT2 cell-like signature, consistent with published observations in human lung adenocarcinoma treated with EGFR inhibitors[29]. Upon loss of wild-type *Kras*, which presumably forces *Kras* signaling through the oncogenic allele, treated tumor cells also expressed markers reflective of an AT1 cell state, consistent with observations from other GEMMs[25]. Although our observation relied on genetic knockout of *Kras^{WT}*, we believe this finding may have translational implications for drug-tolerant disease in the setting of pan-KRAS inhibition. We speculate that alveolar cell states are less dependent on KRAS/MAPK signaling, which enables tolerance to KRAS inhibition.

With sustained sotorasib treatment *in vivo*, we reproducibly generated resistant autochthonous tumors. Without additional genetic perturbation, these tumors universally restored MAPK signaling by amplification of oncogenic *Kras^{G12C}*, testifying to the oncogene addiction of these tumors. Mechanistically, we found that *Kras* amplification occurred through structural rearrangements and ecDNAs. This mechanism has clear

clinical implications. Unlike linear amplifications, which generally segregate equally in daughter cells, ecDNAs do not contain centromeres, and, therefore, can rapidly increase or decrease in copy number in a given cell division[43,71]. In patient tumors, this dynamism could rapidly promote drug resistance in the setting of targeted KRAS inhibition or alleviate oncogene-induced senescence in the context of drug withdrawal. A caveat to this observation is the constitutive expression of Cas9 in our system, which may catalyze off-target double stranded breaks that facilitate ecDNA generation. Notably, the control sgRNA (sg*Olfr*) used does not target the chromosome containing *Kras* (chr6), but we cannot exclude the possibility that unintended Cas9 activity facilitated *Kras* ecDNAs.

In an effort to model histologic transformation, we found that *ΔNp63* upregulation was sufficient to rewire alveolar organoids towards squamous identity *in vitro*, conferring decreased dependence on KRAS signaling and driving a basal airway cell expression signature at the transcriptional level. However, ectopic expression of *ΔNp63* in autochthonous tumors suppressed tumorigenesis, suggesting some form of incompatibility between competing oncogenic lineage programs. While we did not explore the mechanism of tumor suppression deeply, we observed decreased expression of oncogenic KRAS in ΔNp63-expressing organoids, as well as absent pERK in squamous transplanted tumors. We therefore speculate that *ΔNp63*-mediated suppression of *Kras* may impair tumorigenesis. Lineage-specific incompatibilities between oncogenic drivers have been explored in preclinical models of NSCLC to neuroendocrine SCLC transitions, and may explain the prevalence of histologic transformations in patients treated with targeted oncogene inhibition[72].

To model adeno-to-squamous lineage transformation in an autochthonous model, we hypothesized squamous lineages emerge from tumor cells with high effective lineage plasticity. We first tried to model this plastic cell state by overexpressing the lineage transcription factor *Sox2*. Unlike *ΔNp63*, *Sox2* expression did not suppress *Kras*-driven tumorigenesis, and SOX2 may poise cells for squamous lineage commitment upon KRAS inhibition. While we reproducibly observed sotorasib-resistant SOX2^{OE} tumors, these were rarely squamous-transformed. We were most successful in modeling sotorasib-induced squamous transformation through genetic deletion of *Nkx2-1*, a lineage-defining transcription factor for alveolar type II cells. We observe these events in roughly 30% of mice treated for over 10-12 weeks, though it is possible that the incidence would increase with prolonged dosing. Like organoid-derived squamous tumors, these exhibited minimal signaling through MAPK and did not harbor *Kras*^{G12C} amplifications, suggesting oncogene independence. Combining *Nkx2-1*^{KO} with *Sox2* expression, we generated adenosquamous tumors independent of KRAS inhibition. This result may provide insight into the transcription factor dynamics required for histologic transformation. While we found that sotorasib treatment promoted alveolar differentiation upon acute oncogene inhibition, it is possible that the inability of *Nkx2-1*^{KO} cells to access an alveolar drug-tolerant persister state promotes alternative lineage trajectories. In cells with a developmental history of *Sox2* expression, including bronchiolar cells and club cells, this may promote differentiation towards basal

progenitors. In line with this hypothesis, we found that tumor initiation specifically in *Scgb1a1*$^{+}$ cells increased the rate of *Sox2*-mediated histologic transformation, although definitive conclusions are limited by relatively small numbers. Further study is required to determine if all transformed cells in the lung have an equal capacity for histologic transformation, or if developmental origin constrains lineage transition.

Although adeno-to-squamous transitions have been described in patients treated with KRAS, EGFR, and ALK inhibitors, this phenomenon remains poorly understood as a mechanism of resistance to targeted therapy. Our work modeling adeno-to-squamous transitions is not the first preclinical demonstration of squamous differentiation upon KRAS inhibition. Elegant work from Ji and colleagues has implicated *STK11* mutation status as a predictor of baseline adenosquamous histology and propensity towards adeno-to-squamous histologic transformation. Sophisticated preclinical studies using *Kras*/*Lkb1* mutant GEMM models have captured this transition and demonstrated KRAS inhibitor resistance. These studies clearly show that *STK11* loss can be sufficient to promote lineage plasticity, but precisely how *STK11* loss poises tumors for squamous differentiation remains an open question. As we demonstrate, *STK11* loss is not necessary for squamous transformation. While *STK11* status may serve as a risk stratifier for squamous HT, it is notable that *STK11* mutations are almost never detected in *EGFR/ALK* mutant NSCLC, a subset of which also undergo adeno-to-squamous histologic transformation upon TKI resistance. It is possible that like SOX2 activation or NKX2-1 deficiency, *STK11* loss poises the tumor epigenome to access squamous cell states. Preclinical work from Winslow and colleagues has demonstrated that *Kras*^{G12D}*/Stk11*$^{-/-}$ mutant tumors express *Sox17*, which corresponds with divergence from alveolar identity and is necessary for metastasis[73]. Many of these Sox family transcription factors (SOX2, SOX15, SOX17) bind to redundant motifs across the genome, and may have similar capabilities in priming HT.

It is notable that we did not observe neuroendocrine histologic transformation despite sustained treatment and *Rb1* loss. Although there are reports of pretreatment KRAS^{G12C}-mutant lung cancer with neuroendocrine histology[74], we are not aware of confirmed drug-induced small cell lineage transformations in patients treated with KRAS inhibitors. It is an open question as to whether the biology of KRAS-driven lung cancer is fundamentally different in a way that precludes neuroendocrine transformation. EGFR-mutant lung cancer patients are more likely to have pre-existing *RB1* mutations, which are seldom observed in KRAS-mutant lung cancer. This may partially account for the discrepancy seen in EGFR- vs KRAS-driven lung cancer patients, but our data suggest that even engineered *Rb1* loss in *Kras*-driven GEMMs does not enable neuroendocrine transformation. It is possible, given the relatively long latency of the *Trp53*$^{fl/fl}$*;Rb*$^{fl/fl}$ small cell lung cancer GEMM[75], that 12 weeks of sotorasib treatment is insufficient for lineage transformation to SCLC, and may require additional other oncogenic driver events (e.g. MYC). These remain open questions which will benefit from further characterization of acquired resistance to KRAS inhibitors.

It is important to note certain limitations of the present study. First, the genetics of GEMMs are relatively simple compared to complex genotypes observed in human tumors, and therefore, we may have failed to capture the full spectrum of tumor intra- and intertumoral heterogeneity. At the time of this publication, neither sotorasib nor any KRAS inhibitor is first-line therapy for KRAS-mutant NSCLC. It is possible that first-line chemotherapy and/or immunotherapy increase intratumoral heterogeneity and contribute to lineage plasticity that is not captured by administering sotorasib monotherapy. Second, while we successfully reproduced drug-induced histologic transformation in the mouse, these lineage changes often emerged after many months of targeted therapy treatment. For practical considerations, we did not extend sotorasib treatment experiments beyond 12 weeks. In this regard, genetic approaches may be more practical and cost effective for studying the effects of prolonged KRAS inhibition, though these can be susceptible to various escape mechanisms[25]. Finally, while we were able to model adeno-to-squamous transformation in response to KRAS inhibition, it remains a relatively rare event in our hands, even with extensive genetic engineering. We expect that these models will provide a platform for further mechanistic studies that will inform next-generation models of this important form of targeted drug resistance.

Acknowledgments:

We thank members of the Jacks laboratory, notably Zack Ely, Sean-Luc Shanahan, Christina Cabana, and Geoff Smith for intellectual contribution and technical support. We thank Yadira Soto-Feliciano, Francisco Sanchez-Rivera, Colin Fowler, Chris Nabel, and Catherine Meador for helpful discussions and feedback on the manuscript. We thank Roderick Bronson for pathologic confirmation of squamous histology. We thank Judy Teixeira, Karen Yee, Kim Mercer, Kate Anderson, and Margaret Magendantz for administrative and technical support. This work was supported in part by the Koch Institute Support (core) Grant P30-CA014051 from the National Cancer Institute. We thank the Koch Institute's Robert A. Swanson (1969) Biotechnology Center for technical support, specifically the Animal Imaging and Preclinical Testing Core and the Hope Babette Tang Histology Core, including Kathleen Cormier, Danielle Hardie, Tuan Luo, and Charlene Condon. N.M.A received fellowship support from F30CA278495 (Ruth Kirschstein National Service Research Award), which supported this study prior to NIH termination. D.Y. received support from Damon Runyon Dale Frey Award, NCI Transition Career Development Award 1K22CA289207, NIH Director's New Innovator Award 1DP2OD037078 and Lung Cancer Research Foundation Leading Edge Award. C.P.C receives external support from the Lung Cancer Foundation, NIH/NCI R37CA300526, the Department of Defense Lung Cancer Research Program HT9425-25-1-0108, the Gilead Sciences Research Scholar Program, and Prelude Therapeutics. B.S. is supported by a Jane Coffin Childs Fund Postdoctoral Fellowship. A.L.P. was supported by F99/K00 Predoctoral to Postdoctoral Fellowship from the National Cancer Institute (K00CA253687). This work was also supported by T32GM136540 and the Ludwig Center at MIT.

Author contributions:

N.M.A. and T.J. conceived of the study. N.M.A, C.L.R., B.S. performed autochthonous tumor modeling and drug treatment. N.M.A, C.L.R., D.Y., A.L.P, B.S., M.G.H., W.M.R., performed additional experiments. V.Z.C. and I.M. helped perform scRNA sequencing analysis. M.C.B. assisted with μCT data collection and wrote scripts for μCT image analysis. M.L. and C.P.C. provided USCC vector and experimental feedback. N.M.A. and T.J. wrote the manuscript with input from all authors.

Declaration of Interests:

N.M.A. has served as an Ad Hoc consultant for Longitude Capital on matters unrelated to the content of this manuscript. D.Y. is a co-founder and consultant for DEM Biopharma. T.J. is a member of the Board of Directors of Amgen and Thermo Fisher Scientific, a co-Founder of Dragonfly Therapeutics and T2 Biosystems. Amgen currently owns and markets sotorasib, the primary therapeutic compound used in this manuscript. Sotorasib was purchased from a third-party source, Selleck Chemicals, and the work was not performed as a sponsored research agreement. T.J. serves on the Scientific Advisory Board of Dragonfly Therapeutics, SQZ Biotech, and Skyhawk Therapeutics. T.J. is also the President of Break Through Cancer. His laboratory currently receives funding from the Lustgarten Foundation and Johnson & Johnson Lung Cancer Initiative, but this funding did not support the research described in this manuscript. The remaining authors declare no competing interests.

Methods:

Lung organoid culture and transplantation.

Lung organoids were derived from 6–12 week-old mice[76]. Lungs were harvested and minced in 100 μl Dispase (Corning), and supplemented with 1-2 mL digestion buffer containing Advanced DMEM/F-12, Penicillin/Streptomycin, Amphotericin B, 1 mg/mL Collagenase (Sigma, C9407-500MG), 40 U/mL DNase I (Roche, 10104159001), 5 μM HEPES, and 0.36 mM $CaCl_2$. Digestion occurred over a 30-minute incubation at 37 ºC in a hybridization oven. The resulting suspension was incubated in 1 mL ACK Lysis Buffer (Thermo, A1049201) for 3-5 minutes at room temperature to lyse red blood cells, passed through a 70 μm filter, and washed with FACS buffer (1X PBS with 1 mM EDTA and 0.1% BSA). Epithelial cells were enriched using the EasySep™ Mouse CD45 Positive Selection kit (STEMCELL technologies, 18945), retaining supernatant instead of the bead bound fraction. Surface stains for flow sorting included: anti-mouse CD31-APC (1:500, Biolegend, 102507), CD45-APC (1:500, BD Biosciences, 559864), EpCAM-PE (1:500, Biolegend, 118206), MHCII-FITC (1:100, Thermo, 47-5321-82). A BD FACSAria III Cell Sorter III was used to sort for $DAPI^-$, $CD31^-$, $CD45^-$, $EpCAM^+$, $MHCII^+$ cells, previously published markers for AT2 cells. At least 100,000 sorted AT2 cells were mixed with Growth Factor Reduced Matrigel (Corning) seeded onto multi-well plates as 20μl domes (20,000 cells per 20 μl dome). Organoids were then supplied with F^7NHCS medium supplemented with Y-27632 (Cayman).

Transplantation of organoids[76] was performed in syngeneic recipient mice aged 8-12 weeks. All transplanted organoid lines were derived from female mice to enable transplantation into both male and female recipients. LSL-dCas9VPR mice were used as recipients to ensure tolerization and prevent immunologic rejection to peptides from the dCas9-VPR machinery. Recipients were pretreated intratracheally with 0.1 mg/kg bleomycin 48h before organoid harvest to improve engraftment. Upon transplantation, organoids were dissociated, counted, and 100,000 cells were transplanted per mouse.

Production of lentivirus and transduction.

Lentivirus was produced by transfection of the expression vector into Lenti-X cells (Takara) along with psPAX2 (psPAX2 was a gift from Didier Trono - Addgene plasmid # 12260 ; http://n2t.net/addgene:12260 ; RRID:Addgene_12260) and pMD2.G (pMD2.G was a gift from Didier Trono - Addgene plasmid # 12259 ; http://n2t.net/addgene:12259 ; RRID:Addgene_12259) packaging plasmids at a 4:3:1 ratio using polyethylenimine or Mirus transfection reagent. Quantification of lentiviral titer was performed using a GFP Cre reporter 3TZ cell line[77].

Tumor initiation by intratracheal viral delivery.

Mice were anesthetized in an isoflurane chamber. For Ad-5-SPC experiments, 1 x 10^8 or 2.5 x 10^8 PFU were used (University of Iowa). For lentivirus-initiated tumors, 10,000-25,000 titer units (TU) were used per mouse, as determined by the GFP Cre reporter assay. Mice were sex and age matched within 4 weeks across experimental arms.

Animal studies.

All mouse experiments described in this study were approved by the Massachusetts Institute of Technology Institutional Animal Care and Use Committee (IACUC) (institutional animal welfare assurance no. **A-3125-01**). *Kras$^{LSL\text{-}G12D}$*, *Kras$^{LSL\text{-}G12D}$, LSL-Cas9-P2A-eGFP, LSL-dCas9VPR-P2A-mNeonGreen,* and *Trp53$^{flox/flox}$* mice have previously been described[22,46,78–80]. *LSL-Kras^{G12C}* mice were produced from C57Bl/6J mouse embryonic stem cells derived from a *LSL-KrasG12D*, *Trp53$^{fl/fl}$* strain, following methods published by Zafra et al[81]. Correctly targeted ESC clones were injected into Albino B6 blastocysts. High degree chimeras were chosen for germline transmission, which was confirmed by PCR. All mice were maintained on a pure C57Bl/6J background. Mice between 7-12 weeks old were designated for *in vivo* tumor initiation. Mice of both sexes were used. Mice were assessed for morbidity according to guidelines set by the MIT Division of Comparative Medicine and were humanely sacrificed prior to natural expiration. Sotorasib was formulated in 2% HPMC, 1% Tween80 and delivered daily by oral gavage at 30 mg/kg. Preparations of sotorasib were kept at 4˚ C for a maximum of 2 weeks.

Rodent *μ*CT

Mice were anesthetized by Isoflurane (3%, then maintained at 2.0-2.5% in oxygen – VetEquip, Livermore, CA) and scanned in a prone position using a Skyscan 1276 (Bruker Corp, Billerica, MA) with the following parameters: 100kVp source voltage, 200 uA current, 0.5mm Aluminum X-ray filter, 108ms exposure time, 0.65 degree rotational step size over 360 degrees in a continuous rotation. With 4x4 detector binning, the nominal pixel size after reconstruction (Bruker NRecon software) was 40.16 micron. Data were visualized using ImageJ. Quantification of aerated lung volume was performed using custom Matlab scripts.

Histology, immunohistochemistry, and immunofluorescence.

Tumor-bearing lungs were washed in cold PBS and separated into separate lobes. Tissue was fixed in 4% paraformaldehyde overnight, transferred to 70% Ethanol, and then embedded in paraffin. Hematoxylin and eosin (H&E) staining was performed and digitally scanned images of H&E slides were obtained with an Aperio ScanScope at 20X magnification. Histologic quantification of tumor grade was performed by an automated deep neural network available through Aiforia image analysis software with the nsclc_v37 algorithm.

For IHC, slides were deparaffinized, underwent heat-induced antigen retrieval, and were incubated at 4˚ C overnight with primary antibodies. Antigen retrieval was performed using 10 mM sodium citrate buffer (pH = 6) for the following antibodies: anti-NKX2-1 (1:1000, Abcam, ab76013), anti-SFTPC (1:2500, Millipore Sigma, Cat# AB3786), anti-cleaved Caspase 3 Asp175 (1:500, Cell Signaling, 5A1E), anti-CD4 (1:500, Abcam, ab183685), anti-CD8a (1:500, Abcam, ab217344), anti-FOXP3 (1:100, FJK-16s, eBioscience), anti-F4/80 (1:2000, Cell Signaling D2S9R), anti-CD20 (abcam, ab78237, 1:100), anti-pHistone H3 (Ser10) (Cell Signaling Technologies, #9701), anti-ΔNp63 (1:500, Cell Signaling Technologies, E6Q3O), anti-SOX2 (1:500, Cell Signaling Technologies, D9B8N), anti-KRT5 (1:2500, BioLegend, Poly19055), anti-FOXA1 (1:1000, Abcam, ab170933) anti-FOXA2 (1:1000, Abcam, ab108422), anti-Vimentin (1:2000, Cell Signaling, D21H3), anti-UCHL1 (1:100, Millipore Sigma, HPA005993), anti-CGRP (1:2500, Sigma-Aldrich #C8198) , anti-MYCN (1:400, Cell Signaling, D4B2Y), anti-cMYC (1:400, Abcam, ab32072). Antigen retrieval was performed with Borg Rodent Decloaker (BioCare) for the following antibodies: anti-phosphoERK (T202/Y204) (1:250, Cell Signaling, 197G2) anti-phosphoSTAT3 (Y705) (1:400, Cell Signaling, D3A7). ImPRESS anti-Rabbit or anti-Rat horseradish peroxidase and DAB Peroxidase Substrate Kit (Vector) were used to develop slides. Tissues were counterstained with hematoxylin. Slides were digitally scanned and analyzed using QuPath [82]. Human tissue microarrays were purchased from TissueArray (cat #LC10016) and were baked for 1 hour at 60˚C prior to deparaffinization. Determination of LUAD/LUSC was provided by the vendor.

Cas9, SPC, and Hopx immunofluorescence were performed nearly the exact method as immunohistochemistry, without performing HRP-secondary incubation and performing a 10 minute DAPI counter stain for nuclear visualization. IF images were captured on a

TissueGnostics TissueFAXS SL microscope using the 20X objective, and quantifications were analyzed using the TissueGnostics StrataQuest analysis software.

Western Blotting

Lung tumor organoids were dissociated with Corning Cell Recovery Solution for 30 minutes on ice, washed 2x with PBS, and then lysed in cell lysis buffer (RIPA with 100X HALT protease and phosphatase inhibitors). Blots were incubated with primary antibody HSP90 (1:5000, Cell Signaling, C45G5), tERK (1:2000, Cell Signaling, L34F12), pERK (1:2000, Cell Signaling, 197G2), cleaved Caspase 3 (1:1000, Cell Signaling, 5A1E), cleaved PARP (1:1000, Cell Signaling D214), DUSP6 (1:1000, Abcam, ab76310) NKX2-1/TTF1 (1:1000, Abcam, ab76013) ΔNp63 (1:1000, Cell Signaling Technologies, E6Q3O), SOX2 (1:1000, Cell Signaling Technologies, D9B8N), KRT5 (1:5000, BioLegend, Poly19055), and $KRAS^{G12D}$ (Cell Signaling, 1:1000, D8H7) overnight at 4º in 5% BSA, then stained with HRP-conjugated secondary (Cell Signaling), developed, and imaged on a ChemiDoc Gel Imaging System (BioRad).

Bulk RNA-Sequencing

RNA was isolated from TRIzol lysates using Direct-zol RNA extraction kit (Zymo). A total of 500 ng of RNA was used for polyA capture library preparation (Nextera). Libraries were sequenced at equimolar ratios and raw FASTQ files were evaluated for quality using fastqc. Sequencing reads were aligned using the nextflow nfcore-rnaseq[83] pipeline, aligning reads to the GRCm39 reference. Limma was used for batch correction between mouse organoid lines. DESeq2 was used for differential gene expression and hierarchical clustering.

Single cell RNA sequencing

Individual tumors were plucked and minced in 50 μl Dispase (Corning). 450 μl of digestion buffer (see organoid derivation) was added and tumors incubated for 30 minutes at 37˚ C. After red cell lysis, dissociated tumors were strained through 70 μm mesh filters and stained with the epithelial cell panel (organoid derivation), omitting Class II MHC. Tumor cells were sorted for $eGFP^{+}$, $DAPI^{-}$, $CD31^{-}$, $CD45^{-}$,tumor cells on an BD FACSAria III Cell Sorter, stained with hashing antibodies, and loaded onto a 10X Chromium GEX Chip. Libraries were prepared and sequenced on an Illumina NovaSeq.

Analysis of single cell RNA sequencing

CellRanger 7.0 was used to align and demultiplex FASTQ sequencing reads. Scanpy was used for dimension reduction and visualization. Preprocessing included selection of cells with >200 and <7000 genes, or those with >15% corresponding to mitochondrial genes. Gene expression counts were then log normalized and scaled. Dimension reduction was first performed by PCA including the first 40 principle components, followed by Leiden clustering and UMAP projection. pyGSEA[84] was used for gene set enrichment analysis using gene sets curated by MSigDB[85].

Mouse MSK IMPACT Targeted Sequencing and Analysis

10 μm curls were cut from paraffin-embedded blocks containing resistant tumors and DNA was extracted using the QIAamp DNA FFPE Tissue Kit (Qiagen). DNA was submitted to the MSK Integrated Genomics Operation Core for targeted capture and deep sequencing. This assay captures 578 select cancer genes in the mouse. Sequencing was performed by the MSK Integrated Genomics Operation Core. Raw FASTQ files were evaluated for quality control and processed using the nfcore-sarek pipeline, with custom parameters[83]. Notably, a custom BED file of target genes was used for accurate read mapping. Reads were aligned to GRCm38 using Burrows-Wheeler Aligner v0.7.17 (BWA-MEM). PCR Duplicates were marked using MarkDuplicates. Somatic mutations were called using muTect2[86], Strelka[87], and Manta[88]. CNVs were called using CNVKit[89]. IGV tracks were visualized using recalibrated CRAM files.

Whole genome sequencing:

Tumor DNA was sequenced at 0.5x-10x sequencing coverage for CNV calling using CNV kit. Reads were aligned to GRCm38 using Burrows-Wheeler Aligner v0.7.17 (BWA-MEM). After CNV calls were made, ecDNA detection was performed on tumors sequenced at higher (10x coverage) depth using AmpliconArchitect[40] v1.2, which constructed cyclic paths for corresponding tumors.

Bulk ATAC sequencing

50,000 cells were lysed and tagmented using the Active Motif ATAC Sequencing kit. Libraries were generated using unique i5 and i7 primer combinations for each condition. Fastqc was used to perform quality control on raw FASTQ files, which were aligned to GRCm39 using the nextflow nf-core atacseq pipeline. Hierarchical clustering was performed using DESeq2. Peaks were called using MACS2. Motif analysis was performed with HOMER. Heatmaps were visualized using deepTools. ATAC tracks were visualized using IGV.

Incucyte live cell imaging

Organoids were imaged in a Sartorius Incucyte S3. Organoid area, available under the organoid module, was used to track organoid growth for timecourse experiments. N=2 technical replicates were used in each experiment. Organoids were imaged at 6-hour intervals.

Data availability:

Mouse single cell RNA sequencing, WGS, and bulk RNA/ATAC sequencing will available at GSE*** upon publication.

Supplementary Figure Legends

Supplementary Figure 1.

A. Left: Aiforia quantification of tumor burden comparing KP (n=5, 8, 5 mice for 5, 8, 12, weeks - mice did not survive to 24 weeks p.i. - $Kras^{G12D}$ shown in pink) and

K_cP (n=5, 8, 5, 8 mice for 5, 8, 12, 24 weeks p.i. - $Kras^{G12C}$ shown in blue) mice infected with 10^8 PFU Adeno-SPC-Cre at various timepoints post infection (p.i.). Right: tumor number comparing KP vs K_cP mice per mm^2 of lung, quantified in QuPath.

B. Left: Hematoxylin and eosin (H&E) staining of representative tumor bearing lungs in K_cP mice at 16 or 24 weeks p.i. treated with either 2 weeks of vehicle (n=8, 9, respectively) or 30 mg/kg sotorasib (n=10, 8, respectively). Mice were euthanized at a total of 18 and 26 weeks post tumor initiation. Scale bar indicates 2 mm. Right: Aiforia quantification of tumor burden in K_cP mice at 16 or 24 weeks p.i. treated with either 2 weeks of vehicle or 30 mg/kg sotorasib. Individual unpaired t tests were used to test significance in tumor burden, p values shown above bar plots.
C. Waterfall plots of change in aerated lung volume as calculated by micro-computed tomography (μCT) for mice treated 16 (n = 8 vehicle, n = 10 sotorasib) and 24 weeks (n = 6 vehicle, n = 8 sotorasib) p.i. An increase in aerated lung volume corresponds to a decrease in tumor burden, therefore the axes are flipped for consistency with waterfall plots from clinical studies.
D. Quantification of changes in individual and average tumor volume, determined by μCT, in K_cP mice at 16 weeks p.i. at 0w (16 p.i.), 1w (17w p.i.), and 2w (18w p.i.) following treatment with vehicle or 30 mg/kg sotorasib. Vehicle tumors are shown in red, sotorasib treated tumors are shown in blue. 16 sotorasib treated tumors and 26 vehicle treated tumors are quantified from 6 and 8 mice, respectively.
E. Aiforia quantification of tumor burden in K_cP mice at 16 weeks p.i. treated with either 72h of vehicle or 30 mg/kg sotorasib, n=3 mice per condition. An individual unpaired t test used to test significance in tumor burden, p values shown above bar plots.
F. Phospho Histone H3 (pHH3) quantification of IHC in tumors 18w (n = 9 sotorasib, n = 8 vehicle) and 26w p.i. (n = 8 vehicle, n = 7 sotorasib) treated with vehicle or 30 mg/kg sotorasib, respectively. Statistics were performed on the number of positive cells per mm^2 using individual unpaired two sided t tests. (n = 337 vehicle 18w, 257 vehicle 26w, n = 99 sotorasib 18w, 149 sotorasib 26 weeks)
G. Cleaved Caspase 3 (CC3) quantification of IHC in tumors 18w (n = 9 sotorasib, n = 8 vehicle) and 26w p.i. treated with vehicle or 30 mg/kg sotorasib. Quantification was performed on 240 vehicle and 173 sotorasib treated tumors from (n = 8 vehicle, n = 7 sotorasib) mice, respectively. Two murine SCLC tumor slides (n = 24 tumors) were used as a positive control for CC3 staining (right), demonstrating a relative paucity of apoptotic cells in this model. Statistics were performed on the number of positive cells per mm^2 using individual unpaired two sided t tests.
H. IHC quantification for leukocyte markers (CD8a for CD8, CD20 for B cells, CD4 for CD4 T cells, combined CD4 and FOXP3 for Tregs, F4/80 for macrophages) in tumors 18w and 26w p.i. treated with vehicle or 30 mg/kg sotorasib. Statistics

were performed on the number of positive cells per mm^2 using individual unpaired two sided t tests.

Supplementary Figure 2.

A. Flow cytometry gating strategy for sorting of $eGFP^+$ tumor cells. CD45, CD11b, F4/80, CD31, Ter119 stains were used in an APC dump gate to prevent sorting of leukocytes, macrophages, endothelial cells, and red blood cells. DAPI was used as a live dead marker.
B. Expression of *Hopx, Ager,* and *Clic5* in Leiden clusters from sorted tumor single cell RNA sequencing data depending on coarseness of Leiden clustering. Shown are clustering results from Leiden resolutions of 0.25, 0.5, and 0.75. A resolution of 0.5 was chosen as it captures a population defined by AT1-like gene expression without over-clustering the data.
C. Single cell RNA sequencing gene expression data for cell state annotations as defined by Yang et al[28].

Supplementary Figure 3

A. Left: UMAP embedding from scRNA sequencing of sorted tumor cells color-coded by treatment (sotorasib = blue, vehicle = pink). Right: Feature plot scoring cells for the HALLMARK_KRAS_SIGNALING_UP gene set, with several canonical KRAS signaling marker genes including *Dusp6, Cdkn2a, Cdkn2b.*
B. scRNA sequencing violin plots demonstrating alveolar type II marker genes (*Sftpc, Sftpa1, Lyz2)* across Leiden clusters.
C. Top ranked differentially expressed genes from a pseudobulk analysis comparing sotorasib treated cells to vehicle treated cells. Wilcoxon rank sum test used to determine significance.
D. Heatmaps for alveolar type I and alveolar type II gene signatures enriched in either sotorasib or vehicle treated cells. Cell state signatures determined from Angelidis *et al.*[91], Han *et al.*[92], Strunz *et al.*[93] (mouse), Travaglini *et al.*[26] for human signatures).

Supplementary Figure 4

A. Representative immunofluorescence from K_cP Cas9 mice infected with either USEC-sg*Olfr102* or USEC-sg$Kras^{WT}$ 18 weeks p.i. after 2 weeks of vehicle or 30 mg/kg sotorasib. Green = Cas9, Magenta = Hopx (AT1 marker), Red = pro-SPC (AT2 marker). Scale bars as indicated.
B. Representative H&E staining from the previous experiment demonstrating lepidic histology in sotorasib treated K_cP Cas9 USEC sg$Kras^{WT}$ mice.

Supplementary Figure 5

A. IGV tracks showing mapped DNA sequencing reads from tumor targeted sequencing from a representative sotorasib-resistant K_cP sg*Olfr* tumor. IGV tracks map to *Kras* codon 12, demonstrating an intact $Kras^{G12C}$ mutation

(starred), as well as residues corresponding to the switch II binding pocket (R68, H95, Y96 - starred).

B. CycleViz visualizations of ecDNAs from sotorasib-resistant tumors as annotated by AmpliconArchitect.
C. AmpliconArchitect structural views of 'Complex, Non-Cyclic' amplification of *Kras*^{G12C} in sotorasib resistant tumors.
D. Left: CNV plots for sotorasib-resistant K$_c$P sg*Olfr* tumors. Significant gains and losses are pseudocolored in red and blue, respectively. Focally amplified genes were manually annotated in red. Right: IHC staining for cMYC and MYCN in tumors with focal amplifications in *Myc* and *Mycn*, respectively. Scale bars as indicated.

Supplementary Figure 6

A. Schematic for initiation of short and long term sotorasib treatment experiments of K$_c$P, *Rb1*^{KO} tumors using CRISPR-KO.
B. Representative H&E of lung tumors from an untreated K$_c$P USEC-sg*Rb1* mouse, 18 weeks p.i. demonstrating poorly differentiated adenocarcinoma (left inset), sarcomatoid mesenchymal histology (right). Below: Representative H&E of distal liver and spleen metastases in a K$_c$P Cas9 USEC-sg*Rb1* infected mouse 18 weeks p.i. 'S' indicates spleen and 'L' indicates liver. Scale bars as indicated.
C. pHH3 IHC quantification of K$_c$P Cas9 sg*Olfr* and sg*Rb1* tumors 18w p.i. treated with vehicle or 30 mg/kg sotorasib. Quantifications were performed on the following: sg*Olfr* vehicle: 4 mice (n= 135 tumors), sg*Olfr* sotorasib: 4 mice (n=45 tumors) sg*Rb1* vehicle: 7 mice (n = 306 tumors), sg*Rb1* sotorasib: 5 mice (n=117 tumors). Statistics were performed on the number of pHH3-positive cells per mm^2 with a two-way ANOVA.
D. Aiforia quantification of tumor burden (%G2-G4) of K$_c$P Cas9 mice infected with USEC sgOlfr or USEC sg*Rb1* 18 weeks p.i. after 2 weeks of vehicle (pink, n=6, 10, respectively) or 30 mg/kg sotorasib (blue, n=7, 10, respectively). Individual unpaired t tests were used to test for significance.
E. Copy number profiles for chromosome 6 indicating focal amplification of *Kras*^{G12C} in resistant K$_c$P *Rb1*^{KO} tumors (n = 7).
F. CNV profiles from resistant tumors (T1, T2) with and without focal *Kras*^{G12C} amplifications, with corresponding pERK immunohistochemistry.

Supplementary Figure 7

A. Violin plots for *EGFR, SFTPC, NKX2-1, KRT5, KRT14, KRT16* in patient TH226, who had EGFR exon 19 deletion-mutant NSCLC treated with osimertinib and exhibited pathology confirmed squamous transformation. scRNA sequencing data obtained from Maynard et al. (PRJNA591860). 'Early' and 'Baseline' correspond to pretreatment and maximal treatment response. 'Late' corresponds to post squamous transformation.

B. RT-qPCR normalized mRNA expression in KP-VPR organoids targeted with sgRNAs to activate candidate transcription factors. qPCR performed 2 passages after USEC transformation. Transcripts normalized to *Gapdh* expression.
C. RT-qPCR for normalized *Kras* expression in KP-sg*Olfr* and KP-sg*ΔNp63* organoids treated with DMSO or 3h 1μM MRTX1133. mRNA normalized to *Gadph*. Proportion of reads corresponding to oncogenic $Kras^{G12D}$ and WT *Kras* by targeted cDNA sequencing. mRNA collected from KP-sgOlfr and KP-sg*ΔNp63* organoids treated with DMSO or 3h 1μM MRTX1133.
D. Cancer Dependency Map scatterplot and Pearson correlation (r = 0.718) comparing TP63 expression to MSigDB HALLMARK_KRAS_DN gene set signature in human squamous cell carcinoma cell lines (n = 26).

Supplementary Figure 8

A. Experimental schematic for KP-VPR organoid transplantation. $Trp53^{fl/fl}$; *LSL-dCas9-VPR* mice were pretreated with 0.25 mg/kg bleomycin to improve engraftment and 100K organoid cells were orthotopically transplanted 3 days later. Tumor burden quantification for recipient mice 10 weeks post transplantation, receiving either KP-VPR sg*Olfr* or sg*ΔNp63* organoids.
B. Representative immunohistochemistry for NKX2-1 and ΔNp63 in tumors that contain both adenocarcinomatous (AdCA, $NKX2\text{-}1^{+}$) and squamous (SCC, $\Delta Np63^{+}$) histology.
C. Immunohistochemistry for phospho-STAT1, phospho-STAT3, phospho-AKT (Thr308), and cMYC in transplanted organoid adenocarcinomas and squamous cell carcinomas. Scale bar indicates 100 μm and is standard for all images.

Supplementary Figure 9

A. Stereoscopic bright field and fluorescence (mNeonGreen) images from K_cP LSL-dCas9-VPR animals infected with USEC-sg*ΔNp63* 18 weeks p.i. Right: H&E and ΔNp63 IHC from an isolated neoplastic lesion, scale bar indicates 200 μm or 50 μm where specified.
B. Schematic and validation for ΔNp63α and SOX2 overexpression vectors with upstream expression of an sgRNA. Below: western blot and flow cytometry validation for U6-sgInert/*Nkx2-1* EFS (mScarlet, ΔNp63α, SOX2) P2A Cre vectors in Cre-reporter 3T3 cells. HSP90 used as a loading control
C. Representative H&Es and IHC from untreated K_cP Cas9 mice infected with ΔNp63α-P2A-Cre overexpression vectors, 18 weeks p.i. Right panels demonstrate weak/intermittent ΔNp63 positivity, with other lineage markers (SOX2, NKX2-1, KRT5) shown below. Scale bar indicates 100 μm for all panels shown.
D. Representative SOX2 and ΔNp63 IHC in vehicle-treated K_cP Cas9-sg*Olfr* animals 18 weeks p.i. Scale bar indicates 50 μm.

Supplementary Figure 10

A. Representative H&Es and IHC from untreated K_cP Cas9 mice infected with SOX2-P2A-Cre overexpression vectors, 18 weeks p.i., with immunohistochemistry of other lineage markers (SOX2, NKX2-1, KRT5) shown below. Scale bar indicates 100 μm for all panels shown.
B. Immunoblotting of alveolar organoids engineered to overexpress SOX2 with other alveolar/lineage markers. HSP90 used as a loading control.
C. Representative H&E and IHC for NKX2-1$^-$, SOX2$^+$ resistant tumors, including poorly differentiated tumors and papillary adenocarcinomas, in K_cP VPR-sg*Sox2* mice treated with 10 weeks of sotorasib (n = 26 weeks total p.i.). Scale bars as indicated.
D. Representative H&E and IHC for KcP VPR mice initiated with USCC vectors (sg*Inert* and sg*Sox2*) 18 weeks p.i. Airways delineated in red 'A's. Scale bars as indicated.
E. IHC demonstrating rare scattered ΔNp63$^+$ cells in untreated USCC-sg*Sox2* infected mice 18 weeks p.i. Scale bar as indicated.

Supplementary Figure 11

A. H&E, immunohistochemistry, and Alcian Blue/Periodic Acid Schiff (mucin) stain for K_cP Cas9 sg*Nkx2-1* tumors. IHC for NKX2-1, pro-Surfactant Protein C (proSPC), and phosphorylated ERK (pERK). Scale bar indicates 200 μm and is standard for all images.
B. Immunoblots for 3 biological replicate K_cP Cas9 organoid lines infected with USEC-sg*Olfr* or USEC-sg*Nkx2-1*. HSP90 used as a loading control.
C. Representative ΔNp63 IHC in vehicle-treated K_cP Cas9 sg*Nkx2-1* or sg*Olfr* mice 18 weeks p.i. Red arrows indicate intermittent ΔNp63$^+$ cells. Scale bar indicates 50 μm.
D. Schematic of treatment timeline for sotorasib in K_cP Cas9 sg*Nkx2-1* mice. 16 weeks p.i. Mice were treated with either 3w vehicle (n = 5) or sotorasib (n = 5), or 2w sotorasib followed by 1w vehicle holiday (n = 6).
E. H&E and Alcian Blue/Periodic Acid Schiff (AB/PAS) stain on mucinous and non-mucinous *Nkx2-1*^{KO} tumors. Right: Qupath pixel classifier used to determine mucinous (AB/PAS$^+$) tumor area.
F. pHH3 IHC quantification in *Nkx2-1*^{KO} tumors 19w p.i. after 3 weeks vehicle, sotorasib (n = 5 mice, 336 tumors) or 2 weeks sotorasib (n = 5 mice, 167 tumors) with 1 week vehicle holiday (n = 6 mice, 234 tumors). ANOVA was used to determine significance.
G. Qupath AB/PAS pixel classifier pixel quantification in tumors. 232 vehicle 18w, 109 sotorasib 18w (2w), 323 vehicle 19w, 180 sotorasib 19w (3w), 214 19w (2w then 1w). ANOVA was used to determine significance.

Supplementary Figure 12

A. Transformed squamous K_cP Cas9 sg*Nkx2-1* tumor after 12 weeks of sotorasib, H&E pictured with KRT5, ΔNp63, SOX2, pERK immunohistochemistry.

B. Representative H&E of adenosquamous histology in untreated UNES-infected mice 18 weeks p.i. Scale bar as indicated.
C. CNV profile from a transformed squamous tumor with a focal *Yap1* amplification.
D. Corresponding active YAP1 immunohistochemistry from the squamous transformed tumor (right) and a resistant adenocarcinoma on the same slide (left).

References:

1. Tan, A. C. & Tan, D. S. W. Targeted Therapies for Lung Cancer Patients With Oncogenic Driver Molecular Alterations. *JCO* **40**, 611–625 (2022).
2. Canon, J. *et al.* The clinical KRAS(G12C) inhibitor AMG 510 drives anti-tumour immunity. *Nature* **575**, 217–223 (2019).
3. Ostrem, J. M., Peters, U., Sos, M. L., Wells, J. A. & Shokat, K. M. K-Ras(G12C) inhibitors allosterically control GTP affinity and effector interactions. *Nature* **503**, 548–551 (2013).
4. Jänne, P. A. *et al.* Adagrasib in Non–Small-Cell Lung Cancer Harboring a KRASG12C Mutation. *New England Journal of Medicine* **387**, 120–131 (2022).
5. Skoulidis, F. *et al.* Sotorasib for Lung Cancers with KRAS p.G12C Mutation. *New England Journal of Medicine* **384**, 2371–2381 (2021).
6. Collisson, E. A. *et al.* Comprehensive molecular profiling of lung adenocarcinoma. *Nature* **511**, 543–550 (2014).
7. Dagogo-Jack, I. & Shaw, A. T. Tumour heterogeneity and resistance to cancer therapies. *Nat Rev Clin Oncol* **15**, 81–94 (2018).
8. Thress, K. S. *et al.* Acquired EGFR C797S mutation mediates resistance to AZD9291 in non-small cell lung cancer harboring EGFR T790M. *Nat Med* **21**, 560–562 (2015).
9. Engelman, J. A. *et al.* MET amplification leads to gefitinib resistance in lung cancer by activating ERBB3 signaling. *Science* **316**, 1039–1043 (2007).
10. Zhu, V. W., Schrock, A. B., Ali, S. M. & Ou, S.-H. I. Differential response to a combination of full-dose osimertinib and crizotinib in a patient with EGFR-mutant non-small cell lung cancer and emergent MET amplification. *Lung Cancer (Auckl)* **10**, 21–26 (2019).
11. Dagogo-Jack, I. *et al.* MET Alterations Are a Recurring and Actionable Resistance Mechanism in ALK-Positive Lung Cancer. *Clin Cancer Res* **26**, 2535–2545 (2020).
12. Niederst, M. J. *et al.* RB loss in resistant EGFR mutant lung adenocarcinomas that transform to small-cell lung cancer. *Nat Commun* **6**, 6377 (2015).
13. Sequist, L. V. *et al.* Genotypic and Histological Evolution of Lung Cancers Acquiring Resistance to EGFR Inhibitors. *Science Translational Medicine* **3**, 75ra26-75ra26 (2011).
14. Schoenfeld, A. J. *et al.* Tumor Analyses Reveal Squamous Transformation and Off-Target Alterations As Early Resistance Mechanisms to First-line Osimertinib in EGFR-Mutant Lung Cancer. *Clin Cancer Res* **26**, 2654–2663 (2020).
15. Awad, M. M. *et al.* Acquired Resistance to KRASG12C Inhibition in Cancer. *N Engl J Med* **384**, 2382–2393 (2021).
16. Zhang, Z. *et al.* Activation of the AXL kinase causes resistance to EGFR-targeted therapy in lung cancer. *Nat Genet* **44**, 852–860 (2012).
17. Tanaka, N. *et al.* Clinical Acquired Resistance to KRASG12C Inhibition through a Novel KRAS Switch-II Pocket Mutation and Polyclonal Alterations Converging on RAS-MAPK Reactivation. *Cancer Discov* **11**, 1913–1922 (2021).
18. Tong, X. *et al.* Adeno-to-squamous transition drives resistance to KRAS inhibition in LKB1 mutant lung cancer. *Cancer Cell* **42**, 413-428.e7 (2024).
19. Ghazi, P. C. *et al.* Inhibition of ULK1/2 and KRASG12C controls tumor growth in preclinical

models of lung cancer. *eLife* **13**, (2024).
20. Ji, H. *et al.* LKB1 modulates lung cancer differentiation and metastasis. *Nature* **448**, 807–810 (2007).
21. Park, S., Han, J. & Sun, J.-M. Histologic transformation of ALK-rearranged adenocarcinoma to squamous cell carcinoma after treatment with ALK inhibitor. *Lung Cancer* **127**, 66–68 (2019).
22. Zafra, M. P. *et al.* An In Vivo Kras Allelic Series Reveals Distinct Phenotypes of Common Oncogenic Variants. *Cancer Discov* **10**, 1654–1671 (2020).
23. Sutherland, K. D. *et al.* Multiple cells-of-origin of mutant K-Ras-induced mouse lung adenocarcinoma. *Proc Natl Acad Sci U S A* **111**, 4952–4957 (2014).
24. Blair, L. M. *et al.* Oncogenic context shapes the fitness landscape of tumor suppression. *Nat Commun* **14**, 6422 (2023).
25. Li, Z. *et al.* Alveolar differentiation drives resistance to KRAS inhibition in lung adenocarcinoma. *Cancer Discov* (2023) doi:10.1158/2159-8290.CD-23-0289.
26. Travaglini, K. J. *et al.* A molecular cell atlas of the human lung from single-cell RNA sequencing. *Nature* **587**, 619–625 (2020).
27. Marjanovic, N. D. *et al.* Emergence of a High-Plasticity Cell State during Lung Cancer Evolution. *Cancer Cell* **38**, 229-246.e13 (2020).
28. Yang, D. *et al.* Lineage tracing reveals the phylodynamics, plasticity, and paths of tumor evolution. *Cell* **185**, 1905-1923.e25 (2022).
29. Maynard, A. *et al.* Therapy-Induced Evolution of Human Lung Cancer Revealed by Single-Cell RNA Sequencing. *Cell* **182**, 1232-1251.e22 (2020).
30. LaFave, L. M. *et al.* Epigenomic State Transitions Characterize Tumor Progression in Mouse Lung Adenocarcinoma. *Cancer Cell* **38**, 212-228.e13 (2020).
31. Feldser, D. M. *et al.* Stage-specific sensitivity to p53 restoration during lung cancer progression. *Nature* **468**, 572–575 (2010).
32. Winslow, M. M. *et al.* Suppression of lung adenocarcinoma progression by Nkx2-1. *Nature* **473**, 101–104 (2011).
33. Sweet-Cordero, A. *et al.* Comparison of gene expression and DNA copy number changes in a murine model of lung cancer. *Genes, Chromosomes and Cancer* **45**, 338–348 (2006).
34. Junttila, M. R. *et al.* Selective activation of p53-mediated tumour suppression in high-grade tumours. *Nature* **468**, 567–571 (2010).
35. McFadden, D. G. *et al.* Mutational landscape of EGFR-, MYC-, and Kras-driven genetically engineered mouse models of lung adenocarcinoma. *Proceedings of the National Academy of Sciences* **113**, E6409–E6417 (2016).
36. Westcott, P. M. K. *et al.* The mutational landscapes of genetic and chemical models of Kras-driven lung cancer. *Nature* **517**, 489–492 (2015).
37. Chung, W.-J. *et al.* Kras mutant genetically engineered mouse models of human cancers are genomically heterogeneous. *Proceedings of the National Academy of Sciences* **114**, E10947–E10955 (2017).
38. Yaeger, R. *et al.* Molecular Characterization of Acquired Resistance to KRASG12C–EGFR Inhibition in Colorectal Cancer. *Cancer Discovery* **13**, 41–55 (2023).
39. Salmón, M. *et al.* Kras oncogene ablation prevents resistance in advanced lung adenocarcinomas. *J Clin Invest* **133**, e164413.
40. Deshpande, V. *et al.* Exploring the landscape of focal amplifications in cancer using AmpliconArchitect. *Nat Commun* **10**, 392 (2019).
41. Paniagua, G. *et al.* KSR induces RAS-independent MAPK pathway activation and modulates the efficacy of KRAS inhibitors. *Mol Oncol* **16**, 3066–3081 (2022).
42. Yan, X., Mischel, P. & Chang, H. Extrachromosomal DNA in cancer. *Nat Rev Cancer* **24**,

261–273 (2024).
43. Lange, J. T. *et al.* The evolutionary dynamics of extrachromosomal DNA in human cancers. *Nat Genet* **54**, 1527–1533 (2022).
44. Wasko, U. N. *et al.* Tumour-selective activity of RAS-GTP inhibition in pancreatic cancer. *Nature* **629**, 927–936 (2024).
45. Keenan, A. B. *et al.* ChEA3: transcription factor enrichment analysis by orthogonal omics integration. *Nucleic Acids Res* **47**, W212–W224 (2019).
46. Freed-Pastor, W. A. *et al.* The CD155/TIGIT axis promotes and maintains immune evasion in neoantigen-expressing pancreatic cancer. *Cancer Cell* **39**, 1342-1360.e14 (2021).
47. Wang, X. *et al.* Identification of MRTX1133, a Noncovalent, Potent, and Selective KRASG12D Inhibitor. *J Med Chem* **65**, 3123–3133 (2022).
48. Koster, M. I., Kim, S., Mills, A. A., DeMayo, F. J. & Roop, D. R. p63 is the molecular switch for initiation of an epithelial stratification program. *Genes Dev* **18**, 126–131 (2004).
49. Senoo, M., Pinto, F., Crum, C. P. & McKeon, F. p63 Is essential for the proliferative potential of stem cells in stratified epithelia. *Cell* **129**, 523–536 (2007).
50. Yang, A. *et al.* p63, a p53 homolog at 3q27-29, encodes multiple products with transactivating, death-inducing, and dominant-negative activities. *Mol Cell* **2**, 305–316 (1998).
51. Laurikkala, J. *et al.* p63 regulates multiple signalling pathways required for ectodermal organogenesis and differentiation. *Development* **133**, 1553–1563 (2006).
52. Quintanal-Villalonga, A. *et al.* Comprehensive molecular characterization of lung tumors implicates AKT and MYC signaling in adenocarcinoma to squamous cell transdifferentiation. *J Hematol Oncol* **14**, 170 (2021).
53. Qin, Z. *et al.* EML4-ALK fusions drive lung adeno-to-squamous transition through JAK-STAT activation. *Journal of Experimental Medicine* **221**, e20232028 (2024).
54. Su, X., Chakravarti, D. & Flores, E. R. p63 steps into the limelight: crucial roles in the suppression of tumorigenesis and metastasis. *Nat Rev Cancer* **13**, 136–143 (2013).
55. Guo, X. *et al.* TAp63 induces senescence and suppresses tumorigenesis in vivo. *Nat Cell Biol* **11**, 1451–1457 (2009).
56. Nagaraj, A. S. *et al.* Cell of Origin Links Histotype Spectrum to Immune Microenvironment Diversity in Non-small-Cell Lung Cancer Driven by Mutant Kras and Loss of Lkb1. *Cell Reports* **18**, 673–684 (2017).
57. Mollaoglu, G. *et al.* The Lineage-Defining Transcription Factors SOX2 and NKX2-1 Determine Lung Cancer Cell Fate and Shape the Tumor Immune Microenvironment. *Immunity* **49**, 764-779.e9 (2018).
58. Tata, P. R. *et al.* Developmental History Provides a Roadmap for the Emergence of Tumor Plasticity. *Developmental Cell* **44**, 679-693.e5 (2018).
59. Mollaoglu, G. *et al.* The Lineage-Defining Transcription Factors SOX2 and NKX2-1 Determine Lung Cancer Cell Fate and Shape the Tumor Immune Microenvironment. *Immunity* **49**, 764-779.e9 (2018).
60. Han, X. *et al.* Transdifferentiation of lung adenocarcinoma in mice with Lkb1 deficiency to squamous cell carcinoma. *Nat Commun* **5**, 3261 (2014).
61. Hong, K. U., Reynolds, S. D., Watkins, S., Fuchs, E. & Stripp, B. R. Basal Cells Are a Multipotent Progenitor Capable of Renewing the Bronchial Epithelium. *Am J Pathol* **164**, 577–588 (2004).
62. Rawlins, E. L. *et al.* The role of Scgb1a1+ Clara cells in the long-term maintenance and repair of lung airway, but not alveolar, epithelium. *Cell Stem Cell* **4**, 525–534 (2009).
63. Chen, Y. *et al.* Club cells employ regeneration mechanisms during lung tumorigenesis. *Nat Commun* **13**, 4557 (2022).

64. Snyder, E. L. *et al.* Nkx2-1 Represses a Latent Gastric Differentiation Program in Lung Adenocarcinoma. *Mol Cell* **50**, 185–199 (2013).
65. Ferone, G. *et al.* SOX2 Is the Determining Oncogenic Switch in Promoting Lung Squamous Cell Carcinoma from Different Cells of Origin. *Cancer Cell* **30**, 519–532 (2016).
66. Araujo, H. A. *et al.* Mechanisms of response and tolerance to active RAS inhibition in KRAS-mutant NSCLC. *Cancer Discovery* (2024) doi:10.1158/2159-8290.CD-24-0421.
67. Edwards, A. C. *et al.* TEAD Inhibition Overcomes YAP1/TAZ-Driven Primary and Acquired Resistance to KRASG12C Inhibitors. *Cancer Research* **83**, 4112–4129 (2023).
68. Prahallad, A. *et al.* CRISPR Screening Identifies Mechanisms of Resistance to KRASG12C and SHP2 Inhibitor Combinations in Non–Small Cell Lung Cancer. *Cancer Research* **83**, 4130–4141 (2023).
69. Mukhopadhyay, S. *et al.* Genome-Wide CRISPR Screens Identify Multiple Synthetic Lethal Targets That Enhance KRASG12C Inhibitor Efficacy. *Cancer Research* **83**, 4095–4111 (2023).
70. Gao, Y. *et al.* YAP inhibits squamous transdifferentiation of Lkb1-deficient lung adenocarcinoma through ZEB2-dependent DNp63 repression. *Nat Commun* **5**, 4629 (2014).
71. Nathanson, D. A. *et al.* Targeted therapy resistance mediated by dynamic regulation of extrachromosomal mutant EGFR DNA. *Science* **343**, 72–76 (2014).
72. Gardner, E. E. *et al.* Lineage-specific intolerance to oncogenic drivers restricts histological transformation. *Science* **383**, eadj1415 (2024).
73. Pierce, S. E. *et al.* LKB1 inactivation modulates chromatin accessibility to drive metastatic progression. *Nat Cell Biol* **23**, 915–924 (2021).
74. Ito, T. *et al.* De Novo SCLC Transformation From KRAS G12C-Mutated Lung Adenocarcinoma With Excellent Response to Sotorasib: A Case Report. *JTO Clin Res Rep* **4**, 100510 (2023).
75. Meuwissen, R. *et al.* Induction of small cell lung cancer by somatic inactivation of both Trp53 and Rb1 in a conditional mouse model. *Cancer Cell* **4**, 181–189 (2003).
76. Naranjo, S. *et al.* Modeling diverse genetic subtypes of lung adenocarcinoma with a next-generation alveolar type 2 organoid platform. 2021.12.07.471632 Preprint at https://doi.org/10.1101/2021.12.07.471632 (2021).
77. Sánchez-Rivera, F. J. *et al.* Rapid modelling of cooperating genetic events in cancer through somatic genome editing. *Nature* **516**, 428–431 (2014).
78. Jackson, E. L. *et al.* Analysis of lung tumor initiation and progression using conditional expression of oncogenic K-ras. *Genes Dev* **15**, 3243–3248 (2001).
79. Platt, R. J. *et al.* CRISPR-Cas9 knockin mice for genome editing and cancer modeling. *Cell* **159**, 440–455 (2014).
80. Marino, S., Vooijs, M., van Der Gulden, H., Jonkers, J. & Berns, A. Induction of medulloblastomas in p53-null mutant mice by somatic inactivation of Rb in the external granular layer cells of the cerebellum. *Genes Dev* **14**, 994–1004 (2000).
81. Zafra, M. P. *et al.* An In Vivo Kras Allelic Series Reveals Distinct Phenotypes of Common Oncogenic Variants. *Cancer Discov* **10**, 1654–1671 (2020).
82. Bankhead, P. *et al.* QuPath: Open source software for digital pathology image analysis. *Sci Rep* **7**, 16878 (2017).
83. Ewels, P. A. *et al.* The nf-core framework for community-curated bioinformatics pipelines. *Nat Biotechnol* **38**, 276–278 (2020).
84. Fang, Z., Liu, X. & Peltz, G. GSEApy: a comprehensive package for performing gene set enrichment analysis in Python. *Bioinformatics* **39**, btac757 (2023).
85. Liberzon, A. *et al.* The Molecular Signatures Database Hallmark Gene Set Collection. *cels* **1**, 417–425 (2015).

86. Benjamin, D. *et al.* Calling Somatic SNVs and Indels with Mutect2. 861054 Preprint at https://doi.org/10.1101/861054 (2019).
87. Kim, S. *et al.* Strelka2: fast and accurate calling of germline and somatic variants. *Nat Methods* **15**, 591–594 (2018).
88. Chen, X. *et al.* Manta: rapid detection of structural variants and indels for germline and cancer sequencing applications. *Bioinformatics* **32**, 1220–1222 (2016).
89. Talevich, E., Shain, A. H., Botton, T. & Bastian, B. C. CNVkit: Genome-Wide Copy Number Detection and Visualization from Targeted DNA Sequencing. *PLOS Computational Biology* **12**, e1004873 (2016).
90. Franzén, O., Gan, L.-M. & Björkegren, J. L. M. PanglaoDB: a web server for exploration of mouse and human single-cell RNA sequencing data. *Database* **2019**, baz046 (2019).
91. Angelidis, I. *et al.* An atlas of the aging lung mapped by single cell transcriptomics and deep tissue proteomics. *Nat Commun* **10**, 963 (2019).
92. Han, X. *et al.* Mapping the Mouse Cell Atlas by Microwell-Seq. *Cell* **172**, 1091-1107.e17 (2018).
93. Strunz, M. *et al.* Alveolar regeneration through a Krt8+ transitional stem cell state that persists in human lung fibrosis. *Nat Commun* **11**, 3559 (2020).

Supplementary Files

This is a list of supplementary files associated with this preprint. Click to download.

- MASupplementaryTables.xlsx
- MASFigscompressed.pdf